European Commission

JRC TECHNICAL REPORTS

Toward an Assessment of the Fitness-for-Purpose of Copernicus Ocean Colour Data

G. Zibordi, J.-F. Berthon, B. Bulgarelli,
E. Canuti, F. Mélin and M. Talone

2018

Joint Research Centre

EUR 29476 EN

EU Science Hub
https://ec.europa.eu/jrc

JRC114207

EUR 29476 EN

Print	ISBN 978-92-79-98110-4	ISSN 1018-5593	doi:10.2760/216231
PDF	ISBN 978-92-79-98109-8	ISSN 1831-9424	doi:10.2760/203446

Luxembourg: Publications Office of the European Union, 2018

How to cite this report: G. Zibordi, J.-F. Berthon, B. Bulgarelli, E. Canuti, F. Mélin and M. Talone, *Toward an Assessment of the Fitness for Purpose of Copernicus Ocean Colour Data*, EUR 29476 EN, 2018. Publications of the European Union, Luxembourg, ISBN 978-92-79-98109-8, doi:10.2760/203446, JRC114207.

Contents

Acknowledgements 2
Abstract 3
1 Introduction 4
2 Assessment of OLCI Radiometric Data in European Seas 5
2.1 Data and Methods 5
2.1.1 Satellite Data 5
2.1.2 *In Situ* Data 5
2.2 Results 6
3 Cross-Comparison of Multi-Mission Ocean Colour Data 11
3.1 Data Sets and Processing 11
3.2 Main Validation Results 12
3.3 Analysis of Validation Results 16
4 Impact of Adjacency Effects in Coastal Data Products 19
4.1 Simulation of Adjacency Effects 19
4.2 Relevance of Adjacency Effects in Satellite Observations 20
4.3 The Adjacency Field Around the Lampedusa Island 22
5 Impact of *In Situ* Instruments Characterizations 24
5.1 Uncertainty Requirements 24
5.2 Uncertainty Estimate for *In Situ* L_w 24
6 Reproducibility of Laboratory Pigments Analysis 26
6.1 Statistical Evaluation 27
6.2 Results 27
7 Conclusions 29
References 31
List of acronyms 34

Acknowledgements

This work is a contribution to *i. Earth Observation Support to Copernicus Climate and Marine Services* (EOSS) funded by the Directorate-General Joint Research Center (DG-JRC) and to *ii. Reference In Situ Data for Calibration and Validation* part of the Administrative Arrangement on Copernicus between the Directorate-General for Internal Market, Industry, Entrepreneurship and SMEs (DG-GROW) and DG-JRC.

Authors

Giuseppe Zibordi, Jean-François Berthon, Barbara Bulgarelli, Elisabetta Canuti, Frédéric Mélin and Marco Talone.

Abstract

The Copernicus Program has been established through the Regulation EU No377/2014 with the objective to ensure long-term and sustained provision of accurate and reliable data on environment and security through dedicated services. Among these, the Copernicus Marine Environment Monitoring Service and the marine component of the Climate Change Service, both rely on satellite ocean colour observations delivering data on water quality and climate relevant quantities such as chlorophyll-a concentration used as a proxy for phytoplankton biomass.

This Report, building on the long-standing experience of the JRC on ocean colour, summarizes a number of recent investigations essential to assess the fitness-for-purpose of Copernicus ocean colour data products. These investigations embrace:

i. The accuracy of radiometry data from the Ocean and Land Colour Instrument (OLCI) on board Sentinel-3a. The assessment is performed relying on geographically distributed *in situ* reference measurements from autonomous systems and dedicated oceanographic campaigns.

ii. Uncertainty analysis of ocean colours radiometry data from a number of international missions. The analysis aims at assessing the potentials for the construction of Climate Data Records (CDRs) from independent missions.

iii. The impact of adjacency effects in coastal data limiting the accuracy of ocean colour radiometry products. The study relies on state-of-the-art radiative transfer simulations and aims at quantifying adjacency effects in space data from sensors exhibiting different signal-to-noise ratios.

iv. Uncertainties affecting *in situ* radiometry data as a result of the lack of comprehensive characterizations of field instruments. This is an attempt to illustrate the fundamental importance of comprehensive radiometric calibrations and characterizations for *in situ* instruments supporting validation activities.

v. Reproducibility of the experimental determination of pigments concentrations for the validation of satellite data products. The analysis documents the differences affecting the quantification of pigments concentrations through the application of equivalent methods by different laboratories.

1 Introduction

The spectral water-leaving radiance L_W or alternatively the derived remote sensing reflectance R_{RS}, indicate the light emerging from the sea retrieved from the top of the atmosphere radiance L_T detected by a satellite ocean colour sensor [see Zibordi et al. 2014]. Spectral values of L_W and R_{RS} are then the primary ocean colour data products applied to determine geophysical quantities such as the near-surface chlorophyll-a concentration (*Chla*) used as a proxy for phytoplankton biomass. Consequently, the accuracy of derived quantities depends on the accuracy of primary radiometric products.

The assessment of L_{WN} is thus a fundamental need for any satellite ocean colour mission to verify the capability to meet uncertainty requirements: i.e., 5% for L_{WN} in the blue-green spectral regions in view of determining *Chla* with an uncertainty better than 35% in oceanic waters.

Figure 1 illustrates the complexity of the ocean colour paradigm that, in addition to satellite data, requires a number of basic components spanning from field reference measurements, radiative transfer and bio-optical modelling, advanced methods for time series analysis. Within such a general context, this work summarizes efforts aiming at supporting the assessment of the fitness-for-purpose of Copernicus ocean colour satellite data products in view of ensuring their confident use in environmental and climate applications.

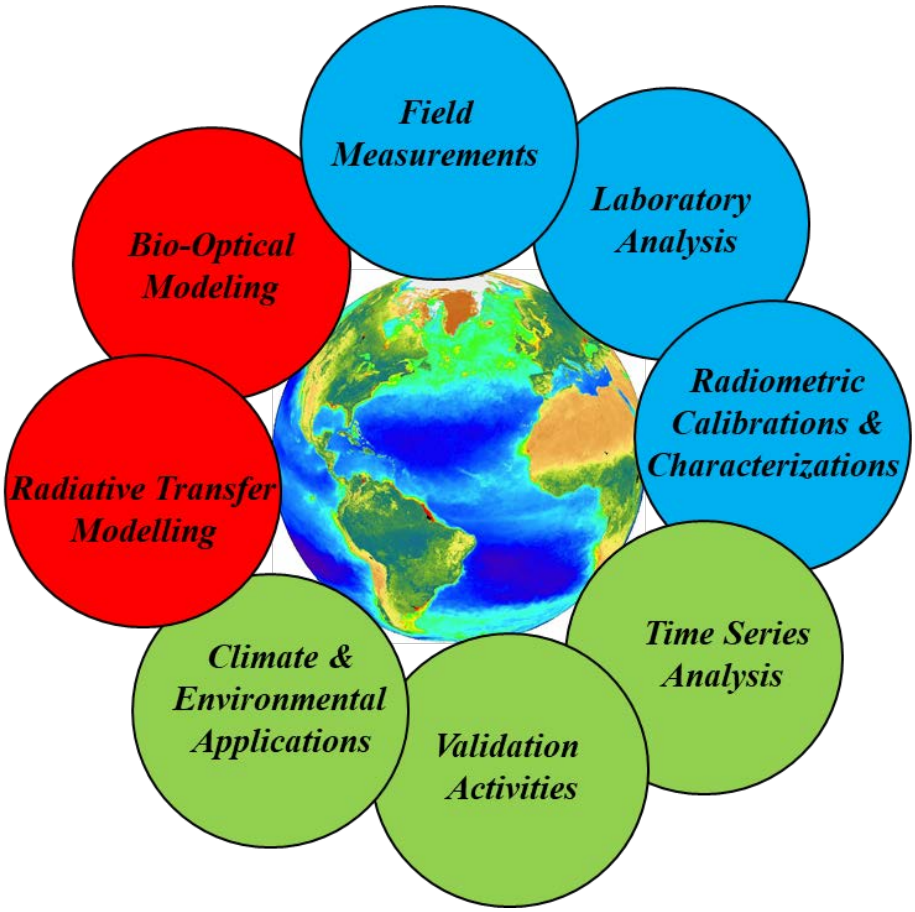

Figure 1. Schematic illustrating the various activities contributing to the development, assessment and exploitation of satellite ocean colour data.

2 Assessment of OLCI Radiometric Data in European Seas [1]

The following analysis focusses on reduced resolution (RR) data from the Ocean and Land Colour Instrument (OLCI) operated on-board Sentinel-3A since February 2016 in the framework of the European Copernicus program. It is mentioned that the same instrument is also active on Sentinel-3B since April 2018 and it will be included in the payload of the following Sentinel-3C and -3D missions.

The objective of this analysis is an assessment of the accuracy of Level-2 ocean colour radiometric products from the Operational Processing Baseline 2.23 applied to OLCI 1.2 km resolution data from April 2016 to November 2017 [EUMETSAT 2018a, 2018b].

2.1 Data and Methods

The validation results presented in this work were obtained from matchups (i.e., quasi coincident *in situ* and satellite data) constructed with a maximum time difference ΔT between *in situ* measurements and satellite overpass. Consistently with previous analysis, satellite RR data were retained for matchup construction when all the 3×3 image elements centered at the *in situ* measurement locations satisfied the following criteria: *i*. data were not affected by cloud contamination and in general by any of the main exclusion flags [EUMETSAT, 2018b]; *ii*. the satellite viewing angle θ was lower than 56° and the sun zenith angle θ_0 lower than 70°; *iii*. the coefficients of variation of L_{WN} at 555 were lower than 0.2.

The matchup analysis was separately performed for different marine regions to investigate differences between *in situ* and satellite data exhibiting diverse dynamics in the radiometric signal as a function of different optical properties of the water.

The comparison results are summarized through *i.* the median of relative (signed) percent differences ψ_m between remote sensing and *in situ* data (as an index for biases), and *ii.* the median of absolute (unsigned) percent differences $|\psi|_m$ (as an index for dispersion). Additional statistical quantities provided to better support the data analysis are the root mean square of differences *rmsd* (with the same units of the quantity considered) and the coefficient of determination r^2.

2.1.1 Satellite Data

The OLCI L_{WN} data, L_{WN}^{OLCI}, assessed in this study were computed from the spectral reflectance ρ^{OLCI} included in the standard Level-2 products, according to

$$L_{WN}^{OLCI} = \rho^{OLCI} \frac{E_0}{\pi} C_{f/Q}$$

where E_0 is the mean extraterrestrial solar irradiance [Thuillier et al. 2003] and $C_{f/Q}$ accounts for the bidirectional effects [EUMETSAT 2018a, Morel et al. 2011].

2.1.2 *In Situ* Data

The *in situ* data applied in this analysis, which are assumed to represent the marine optical properties of a number of European marine regions, are from *i.* the Ocean Colour component of the Aerosol Robotic Network (AERONET-OC) of autonomous radiometers operated at a number of coastal sites [Zibordi et al. 2009] and *ii*. the Bio-optical mapping of Marine Properties (BioMaP) program ensuring the collection of comprehensive shipborne measurements across the various European seas [Zibordi et al. 2011].

[1] This section summarizes some of the finding published in Zibordi et al. 2018.

AERONET-OC data (i.e., L_{WN}) were restricted to Level-2 products exhibiting the highest level of quality assurance [Zibordi et al. 2009] and were confined to five European sites. These are: the Acqua Alta Oceanographic Tower (AAOT, also called Venise) in the northern Adriatic Sea representative of moderately sediment dominated waters; Galata (GLT) and Gloria (GLR) in the Western Black Sea embracing waters dominated by variable concentrations of sediments and colored dissolved organic matter (CDOM); and finally the Gustaf Dalen (GDLT) and the Helsinki (HLT) Lighthouses in the Baltic Proper and in the Gulf of Finland, respectively, representative of highly CDOM dominated waters. The aerosol type is mostly continental with maritime influence at all the sites [Mélin et al. 2013].

The BioMaP data (i.e., L_{WN} and *Chla*) were collected during three oceanographic campaigns performed in *i*. the Western Black Sea (BLKS) onboard the R/V Akademik during June 2016, *ii*. the central Mediterranean Sea (EMED) onboard the R/V Minerva-1 during May 2017, and *iii*. the Iberian Shelf (ISHL) onboard the R/V A.G. Coutinho during September 2017. The aerosol type is continental with maritime influence in the BLKS, maritime with continental influences from various sources in the EMED and maritime in the ISHL [Mélin et al. 2010].

Uncertainties affecting *in situ* L_{WN} data significantly vary from region to region because of the different measurement methods, optical systems, illumination conditions and water type. Specifically, the BioMaP L_{WN} applied in this study were produced with a free-fall profiler and are expected to exhibit uncertainties generally lower than 5% in the blue-green spectral regions and slightly higher in the red [Zibordi et al. 2011]. Conversely, the AERONET-OC L_{WN} determined through above-water radiometry over very different water types, are likely affected by uncertainties largely varying across the various regions with values close to 5% in the blue-green and reaching 8% in the red for the AAOT site, but approaching 30% in the blue at the HLT site [Gergely and Zibordi 2013]. These differences are explained by the choice to quantify uncertainties in relative terms (i.e., in %) and by the very diverse range of L_{WN} characterizing the waters of the various marine regions. For instance, the median of L_{WN} measured at the AAOT in the blue are approximately one order of magnitude higher than that from the HLT values [Gergely and Zibordi 2013].

It is mentioned that the *in situ* L_{WN} applied in the analysis, restricted to the measurements closer in time to the satellite overpass, were band-shifted [Zibordi et al. 2011] to match the OLCI center-wavelengths and consequently minimize the impact of differences between equivalent spectral bands.

2.2 Results

The matchups of *in situ* and satellite L_{WN} data presented in Fig.s 2-5 were constructed applying a maximum time difference ΔT of ±2hr for AERONET-OC data and of ±4hr for BioMaP data. Still, more than 70% of the time differences were within ±1hr for AERONET-OC matchups and approximately 50% were within ±2hr for BioMaP.

The so-called ANNOT flags provided with OLCI data products [EUMETSAT, 2018b] and recommended for validation exercises, were not accounted for in the construction of matchups. In fact, while they do not have any significant impact on the analysis of data from open sea regions like EMED and IHSL, they may lead to the exclusion of a large number of *in situ* – satellite matchups (i.e., from 60 to 90%) for optically complex regions mostly associated with relatively high values of L_{WN}. Still, for the sake of completeness, these matchups are identified by open circles in the scatter plots.

For convenience, the figures illustrating the comparisons are organized by grouping the AERONET-OC data products according to the various marine regions (i.e., the Adriatic Sea, the Black Sea and the Baltic Sea) and conversely, by combining all the BioMaP data regardless of the marine region.

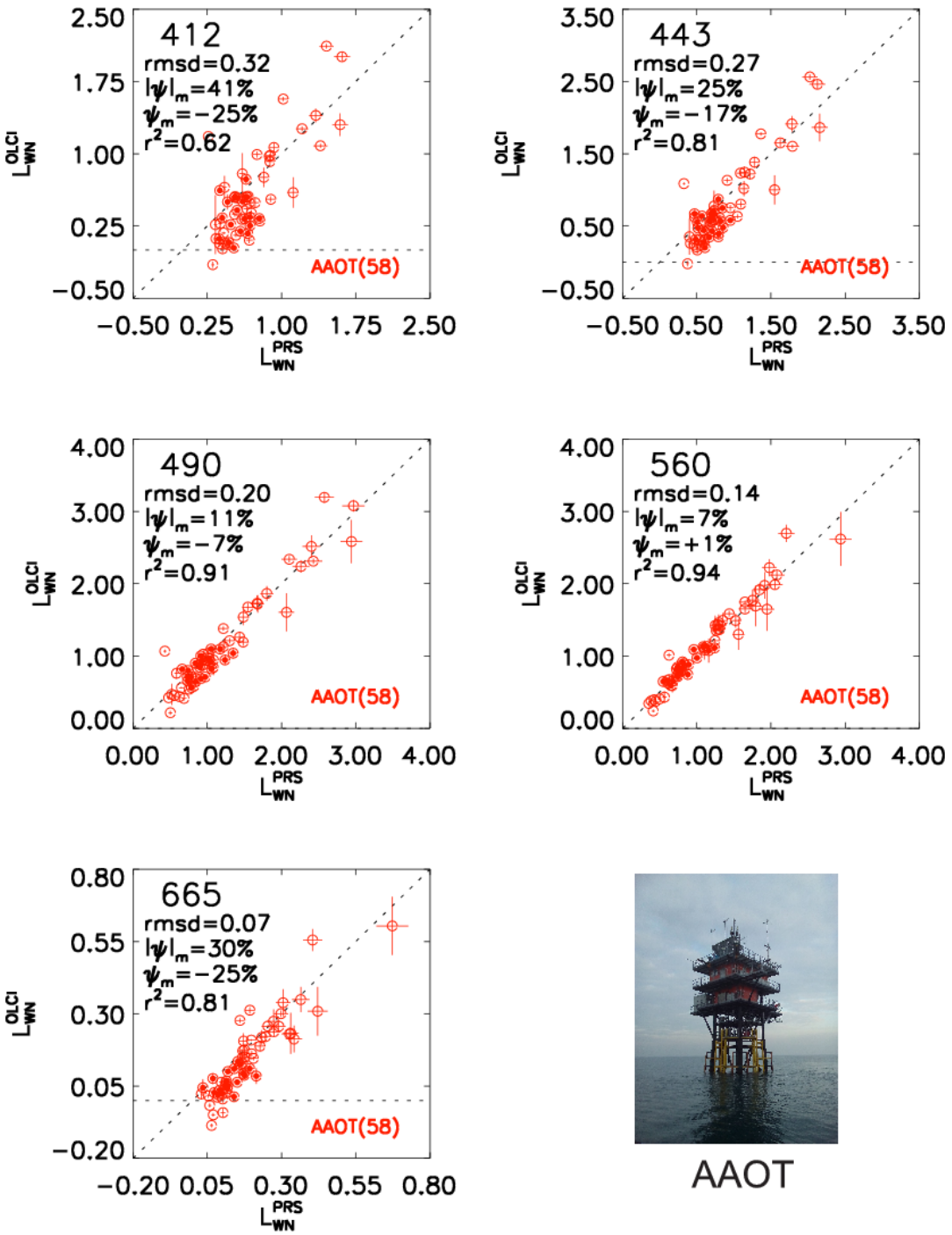

Figure 2. Scatter plots of the AAOT L_{WN}^{OLCI} versus L_{WN}^{PRs} matchup values at 412, 443, 490, 560 and 665 nm. Axes and rmsd are in mW cm^{-2} μm^{-1} sr^{-1}. The semi-filled symbols indicate OLCI data not affected by the ANNOT flags. The error bars on the abscissa indicate the *in situ* measurement uncertainties. Conversely, on the ordinate they indicate the variation coefficients of the 3×3 OLCI elements. The picture illustrates the AAOT infrastructure hosting the AERONET-OC site.

Quantitative comparisons between satellite and *in situ* data are presented in Fig.s 2-5 through individual scatter plots for each spectral band. Notably, the AAOT data in Fig. 2 and the BioMaP data in Fig. 5 do not show any significant impact of negative radiances at the blue bands. However, a high occurrence of OLCI negative L_{WN} data is observed in Fig. 3 for GLT and GLR in the Black Sea.

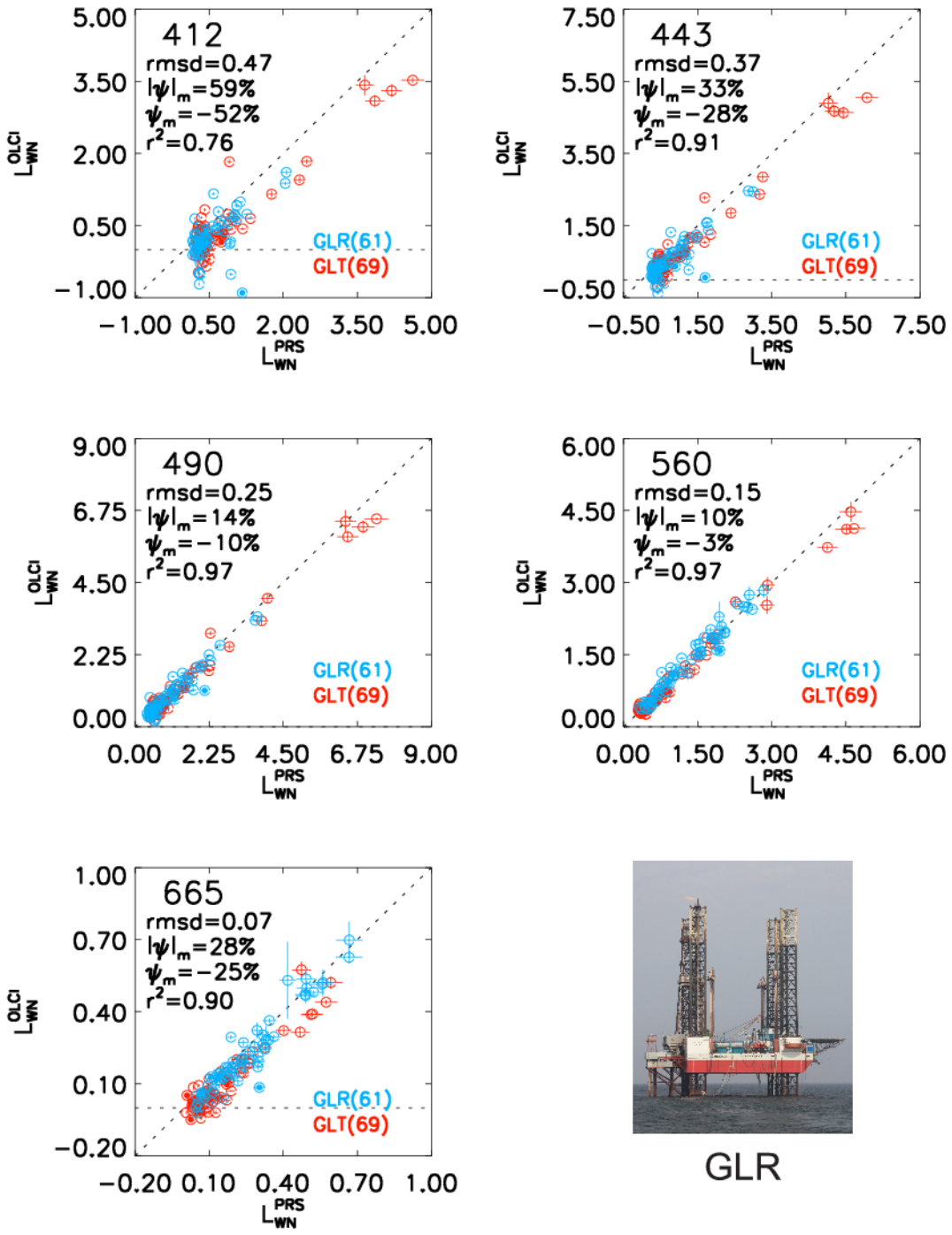

Figure 3. As in Fig. 2 but for the GLT and GLR matchups. The picture illustrates the GLR infrastructure hosting the AERONET-OC site. Colors identify data from different sites.

Specifically, negative L_{WN} appear at 412, 443 and 665 nm. An analysis restricted to the spectra exhibiting those negative radiances, has shown that they mostly pertain to CDOM dominated waters (i.e., exhibiting L_{WN} spectra with maxima at 560 nm, and relative minima at 412 nm and 665 nm). This finding is fully supported by the scatter plots shown in Fig. 4 for GDLT and HLT. Still, regardless of the water type, it is expected that the negative L_{WN} often observed in the Baltic and Black Seas, are the result of an overcorrection of the atmospheric effects.

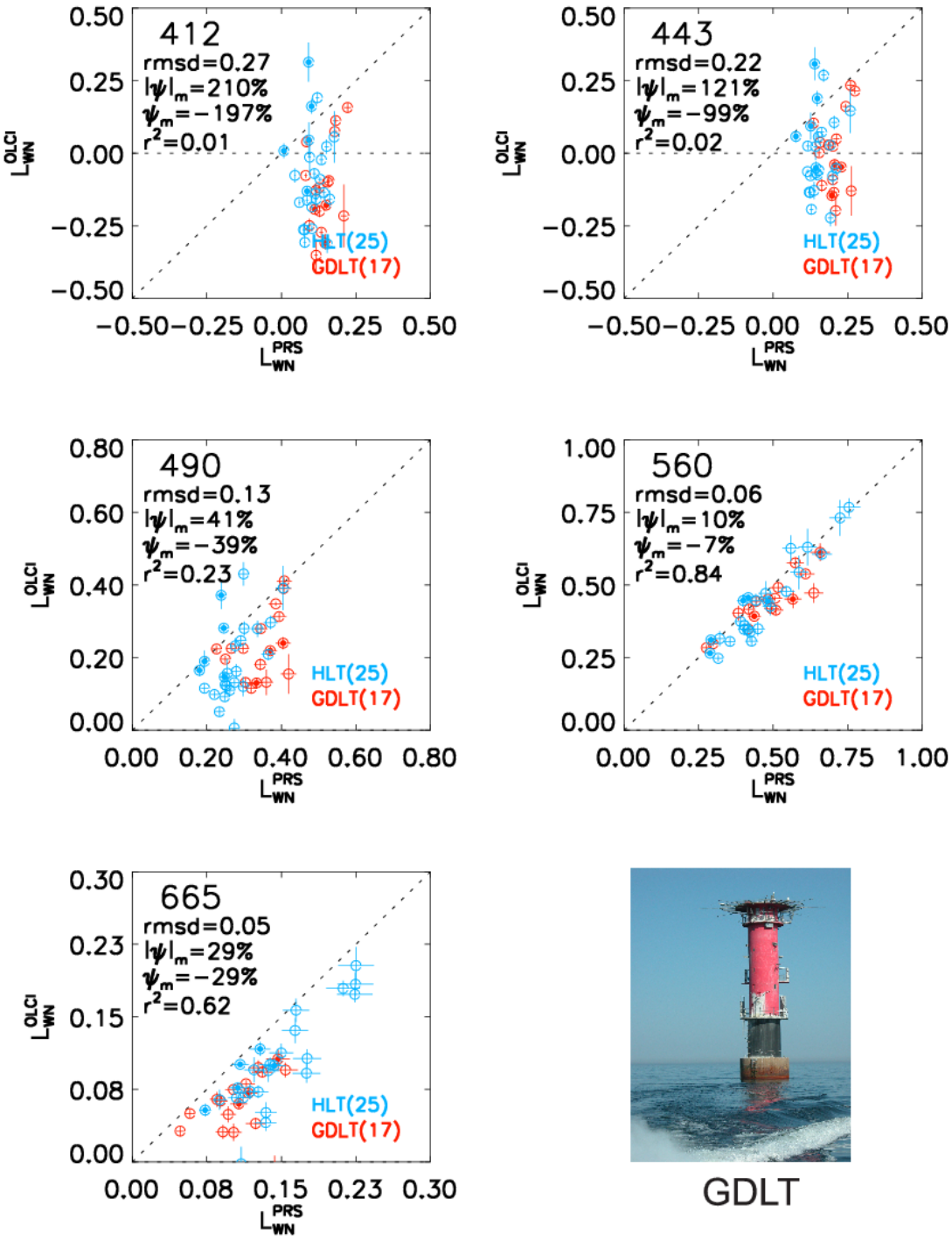

Figure 4. As in Fig. 1, but for the GLDT and HLT matchups. Colors identify data from different sites.

This interpretation is supported by the similarity observed among the scatter plots of τ_a and α proposed for the different marine regions [see Zibordi et al. 2018].

The *rmsd* values determined from the OLCI L_{WN} matchups vary from 0.3-0.5 mW cm^{-2} µm^{-1} sr^{-1} at 412, 0.2-0.4 at 443 nm, decrease to 0.1-0.2 at 490 and 560 nm, and finally exhibit values lower than 0.1 at 665 nm. An evaluation of biases through ψ_m indicates values largely varying with the amplitude of L_{WN}, with minima generally within a few percent at 560 nm except for the BioMaP matchups.

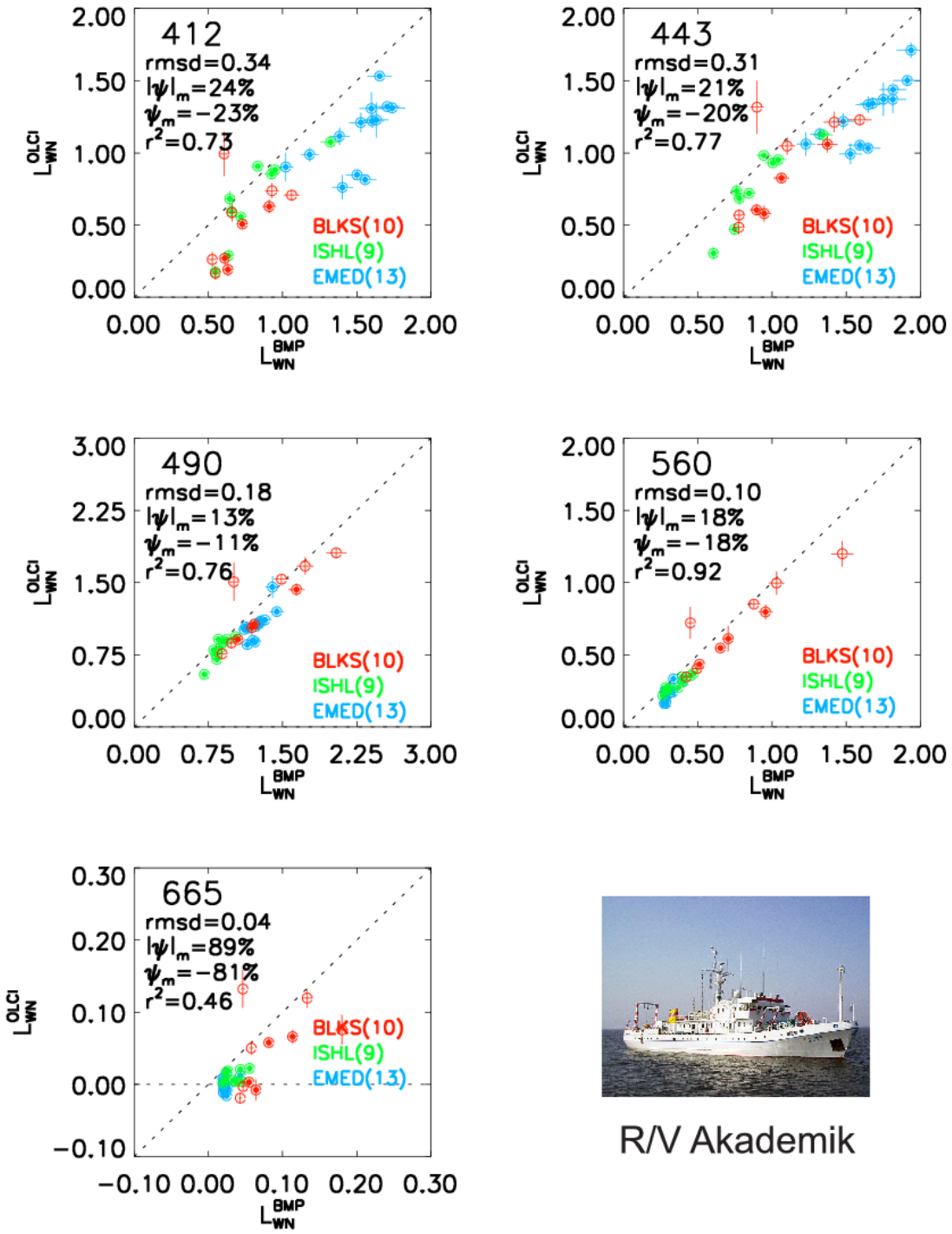

Figure 5. As in Fig. 1 but for the BioMaP-EMED, -IHSL and -BLKS matchups. The picture illustrates the R/V Akademik. Colors identify data from different marine regions.

Overall results from the analysis of L_{WN} indicate a systematic underestimate of OLCI radiometric products equivalent to that reported for the Medium Resolution Imaging Spectrometer (MERIS) Level-2 data from the 3rd reprocessing [Zibordi et al. 2013] largely explained by the equivalent processing codes.

3 Cross-Comparison of Multi-Mission Ocean Colour Data [2]

Mature Climate Data Records (CDR) need uncertainty estimates that are required for various applications. For instance they are needed when data from different satellite missions are combined to create multi-mission time series necessary for climate research, as series from single missions are not long enough to tackle climate issues. After 20 years of operational global ocean colour missions and 16 years of activity of AERONET-OC (introduced in Section 2.1.2), it is possible to take stock of validation results and draw general conclusions on the performance of algorithms applied to global missions. In that context, AERONET-OC data are particularly relevant to assess atmospheric correction algorithms that provide the primary ocean color product, the remote sensing reflectance R_{RS}, equivalent to the normalized water-leaving radiance L_{WN} used in Section 2. The following sections summarize validation results associated with several international missions with the objective of drawing conclusions in terms of R_{RS} uncertainties.

3.1 Data Sets and Processing

The satellite data used for this analysis are part of the data archive maintained by the JRC. The missions considered are the Sea-viewing Wide Field-of-view Sensor (SeaWiFS) onboard a Geoeye spacecraft, the Moderate Resolution Imaging Spectroradiometer (MODIS) onboard the Terra (MODIS-T) and Aqua (MODIS-A) platforms and the Visible/Infrared Imager/Radiometer Suite (VIIRS) onboard the Suomi National Polar-orbiting Partnership (NPP). The archive also contains data from the Moderate Resolution Imaging Spectrometer (MERIS) but these are not included in the analysis to respect a consistency in processing versions. These missions cover the following time frame:

- SeaWiFS: The SeaWiFS mission provided data from September 1997 to December 2010 with some interruptions in the last years. Raw imagery came in two forms. Full resolution data (~ 1.1-km at nadir), or Local Area Coverage (LAC), were collected through receiving stations or recorded on-board for small regions while Global Area Coverage (GAC) data were recorded on-board for global coverage. GAC data are the result of a sub-sampling, so, only LAC are applied here for validation purposes.
- MODIS-T: The MODIS mission on the Terra platform was launched in December 1999 and data have been distributed since February 2000.
- MODIS-A: The MODIS mission on Aqua started providing data in June 2002, with a global coverage at full resolution up to present.
- VIIRS: The NPP platform was launched in October 2011, and VIIRS has been collecting useful data starting in 2012.

For these missions, among other products, the archive contains all Level-1A imagery (L1A, un-calibrated top-of-atmosphere data) covering the European macro-region, including specific imagery associated with AERONET sites (so-called Diagnostic Data Sets, DDS).

To ensure the processing, ancillary data are needed and are included in the archive:

- NCEP ancillary data: atmospheric pressure, relative humidity, precipitable water, zonal and meridional wind speeds (every 6-hour) from the National Centers for Environmental Prediction;
- Ozone concentration: ancillary daily data from various satellite missions
- Geo-reference / attitude files for MODIS-A and MODIS-T (ATTEPH).

[2] This section summarizes finding from Mélin and Zibordi (2018).

Processing of the data to Level-2 is performed with the SeaWiFS Data Analysis System (SeaDAS) software package version 7.3 to produce spectra of R_{RS} for the waveband sets associated to each sensor. The atmospheric correction scheme is based on the work by Gordon and Wang (1994) and subsequent developments (e.g., Franz et al. 2007).

For validation, the AERONET-OC data (Level-2) come from 5 sites already introduced in Section 2.1.2, one in the coastal northern Adriatic (AAOT), two in the Black Sea (GLR, GLT) and two in the Baltic Sea (GDLT, HLT).

The identification of match-ups (coincident field and satellite data) deemed valid for the analysis follows the principles given in Section 2.2 [Zibordi et al. 2009, Mélin et al. 2011]. A 3x3-pixel square centered on the location of the measurement site is extracted from satellite imagery. A match-up is kept for analysis if all 9 pixels are considered valid, i.e. not marked by exclusion flags specific to SeaDAS (related to the presence of clouds, straylight, glint, high zenith angles for observation or illumination, the failure of the atmospheric correction, …). Additionally the time difference between field data acquisition and satellite overpass should not exceed ΔT=1-h, and the Coefficient of Variation (CV, ratio of standard deviation to average) should be below 20% for R_{RS} data. Before comparison between field and satellite data, the field values of R_{RS} are band-shifted as in Section 2.1.2 to match the center-wavelengths of the satellite sensors [Zibordi et al. 2009, Mélin and Sclep 2015].

The following metrics are used for the comparison of field and satellite data:

- Mean absolute relative difference: $|\psi| = 100\frac{1}{N}\sum_{i=1}^{N}\frac{|y_i - x_i|}{x_i}$
- Mean relative difference: $\psi = 100\frac{1}{N}\sum_{i=1}^{N}\frac{y_i - x_i}{x_i}$
- Root-mean Square (RMS) difference: $\sigma = \sqrt{\frac{1}{N}\sum_{i=1}^{N}(y_i - x_i)^2}$
- Mean difference: $\delta = \sum_{i=1}^{N}(y_i - x_i)$
- Centered RMS difference: $\Delta_c = \sqrt{\sigma^2 - \delta^2}$

where N is the number of match-ups, while $(x_i)_{i=1,N}$ and $(y_i)_{i=1,N}$ represent the field and satellite data, respectively. The coefficient of determination r^2 is also computed. The single instance $(y_i\text{-}x_i)$ are called residuals.

As validation results and subsequent analysis for 5 validation sites and 4 multi-spectral missions comprise a large amount of material, only representative examples are illustrated in the following sections.

3.2 Main Validation Results

The main validation results are given here to provide general estimates of differences with field data, to illustrate the distribution of residuals and to see how results change across missions and sites.

Fig. 6 provides an example of scatter plots for the case of MODIS-A at the AAOT site. Using 15 years of coincident data, the number of match-ups is now remarkable (close to 900). From 469 to 555 nm, mean absolute relative differences |ψ| are of the order of 11-13% with a systematic underestimate of approximately 7%. Differences are larger at 412 nm and in the red part of the spectrum. Fairly similar results are obtained for other missions.

Fig. 7 compares validation results (expressed by the RMS difference σ) at all five sites for all missions. It is worth noticing that the number of match-ups varies much across sites and missions. Despite some exceptions (like SeaWiFS at GDLT or MODIS-T at GLT), the spectra of σ show similar results for the different missions for a given site. In Fig. 7, uncertainties associated with field data are also displayed [Gergely and Zibordi, 2014]. In general they are much lower than the RMS differences between field and satellite data, but they get closer in the HLT case (for green-red bands), a Baltic site where R_{RS} values are very low.

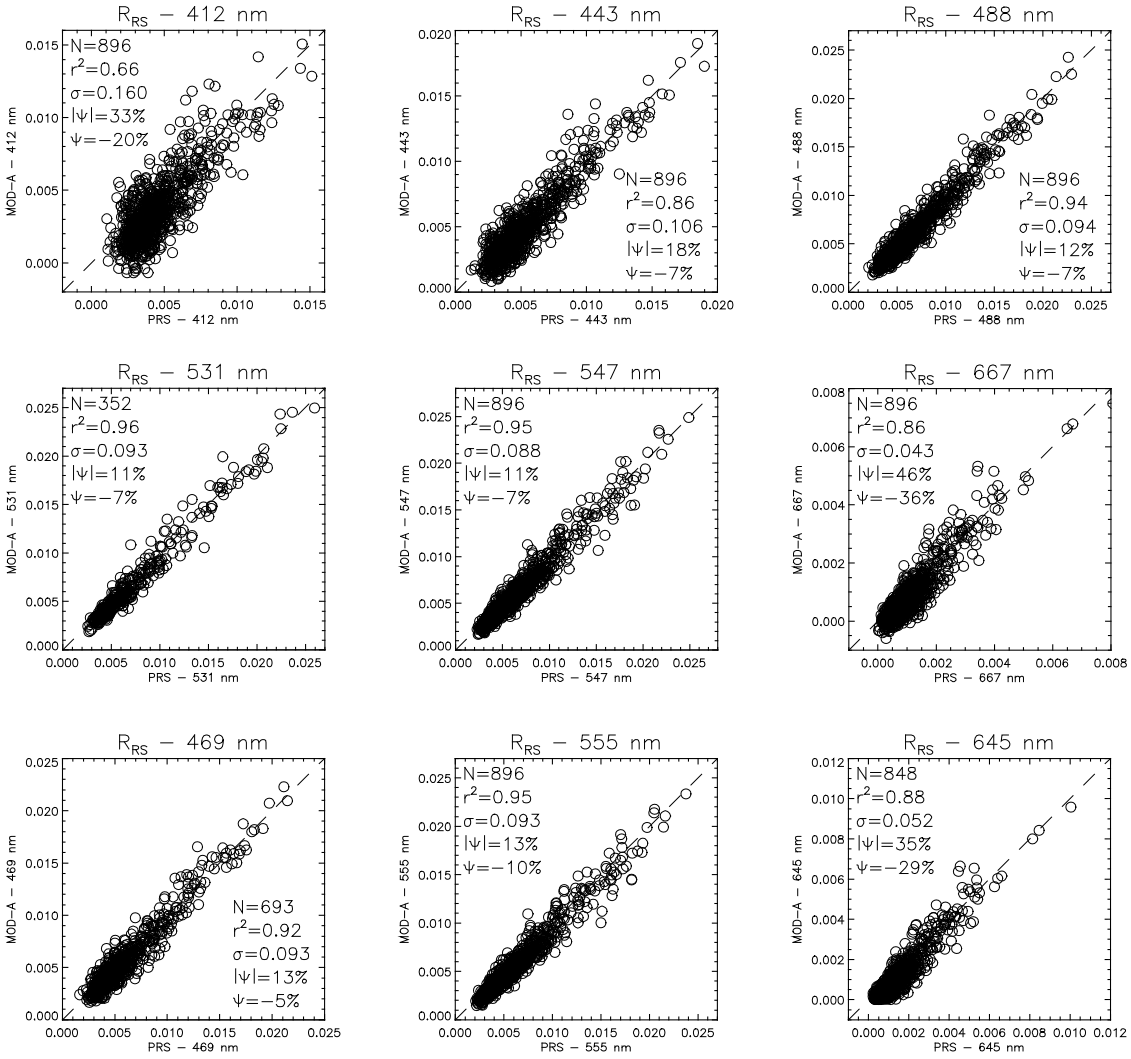

Figure 6. Scatter of R_{RS} obtained from field data (PRS, x-axis) at the AAOT and MODIS-A data. σ (RMS difference) is multiplied by 100 and in units of sr^{-1}.

The same statistics can be represented for a given mission for the different sites to see how they vary through the various locations. The example of VIIRS in Fig. 8 shows that there is quite a variation of results across sites. The mean relative difference |ψ| (Fig. 8a) is much higher in the blue for the two Baltic sites (GDLT and HLT) with respect to the other sites, while it is lower in the red. Results for the 3 other sites are fairly similar with some differences at 671 nm. In the case of the RMS difference σ (Fig. 8b), the highest values are found for the AAOT site, followed by the Black Sea and the Baltic sites (lowest σ). Results obtained in the same region (Baltic Sea or western shelf of the Black Sea) are remarkably close even though there still exist differences in bio-optical properties found at these sites. There is a direct relationship between these results and the magnitude of R_{RS} observed at each location. For instance, R_{RS} values are low in the Baltic Sea, leading to low σ. To the contrary, low values of R_{RS} are associated with high relative differences, particularly at 412-443 nm where the signal is very low. This behaviour is often translated by a horseshoe shape for |ψ|, with minima in the central part of the spectrum and higher values for blue and red bands, all higher for the lower R_{RS}.

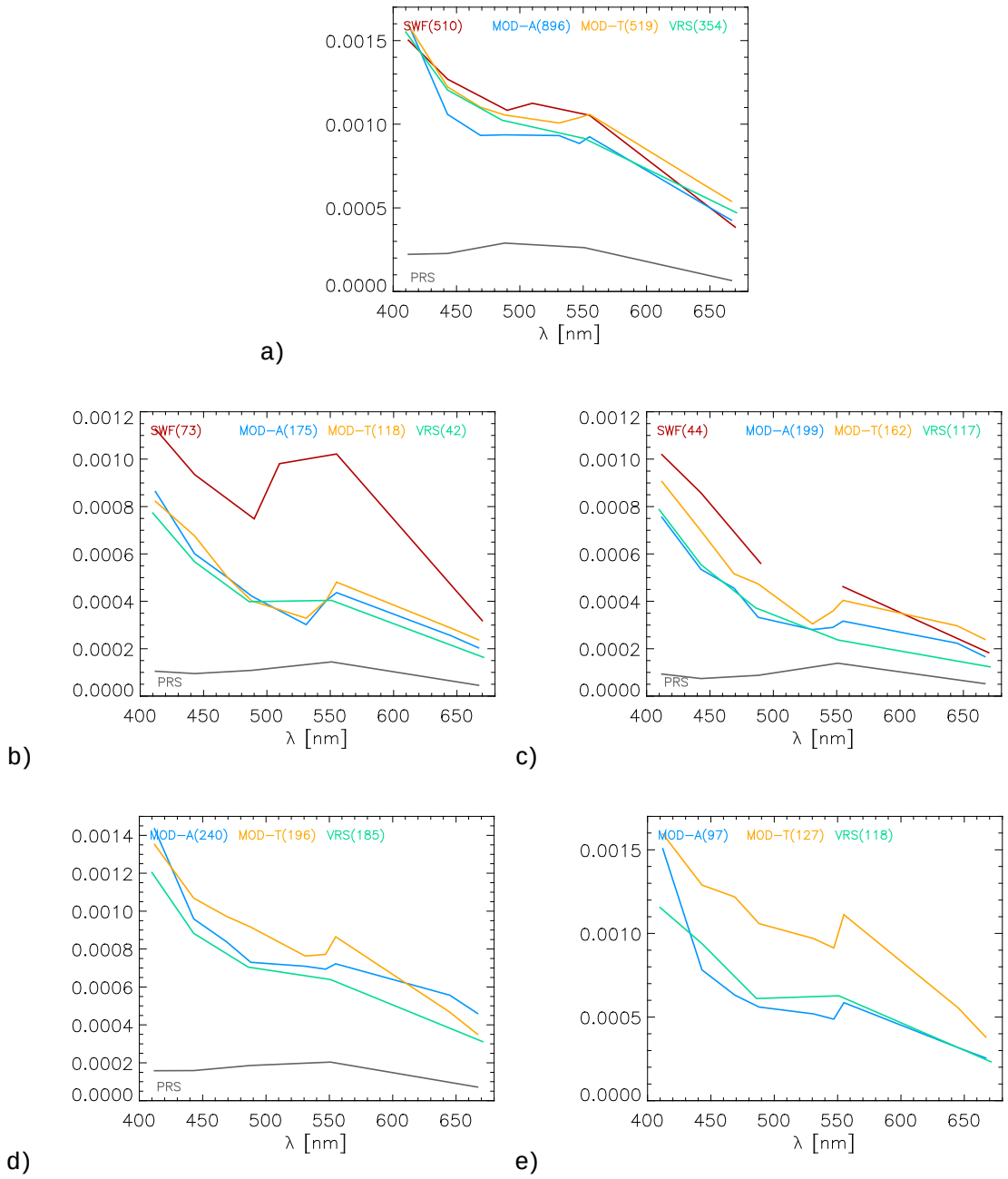

Figure 7. Validation results in terms of RMS difference σ, in units of sr^{-1}, given for the sites a) AAOT, b) GDLT, c) HLT, d) GLR and e) GLT. For each mission, the number of match-ups is given in brackets. The black line (PRS) shows the uncertainty associated with field data (Gergely and Zibordi 2014).

Fig. 9 illustrates the distribution of residuals for MODIS-A with respect to AAOT (in association with Fig. 6) that is fairly representative of results found for other missions and sites. The histograms appear reasonably comparable with Gaussian distributions as confirmed by the overlaying Gaussian function of width Δ_c (centered RMS difference) centered at δ (mean difference). Note that this is not a Gaussian fit to the histogram.

The percentage of residuals observed in the interval $[\delta-\Delta_c; \delta+\Delta_c]$ is found between 72% and 79%, somewhat higher than 68%, which is the expected value for a distribution of residuals perfectly described by the Gaussian function (excess kurtosis). In a hypothesis of normality of the distribution of residuals, Δ_c could be used to represent the shape of this distribution: the present results indicate that interpreting the value of Δ_c in these terms is conservative.

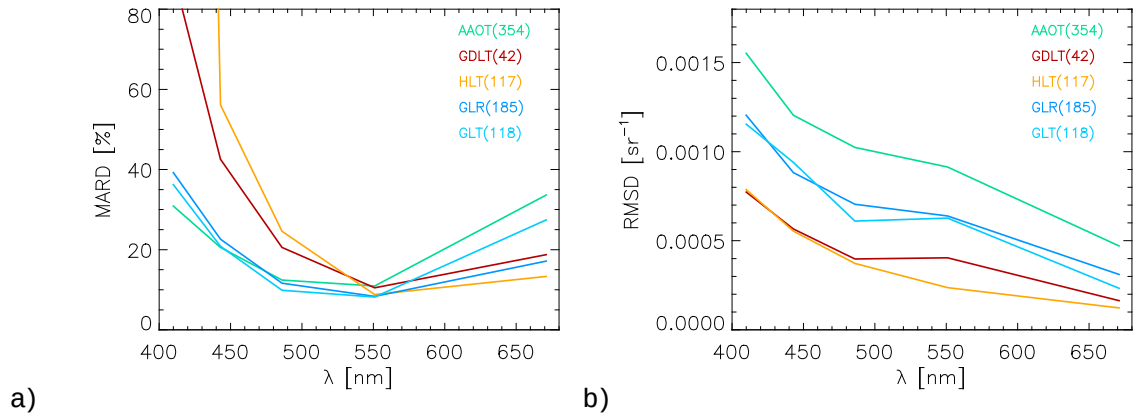

Figure 8. Validation results in terms of a) mean relative difference $|\Psi|$ and b) RMS difference σ, in units of sr^{-1}, given for the 5 sites (with respective number of match-ups).

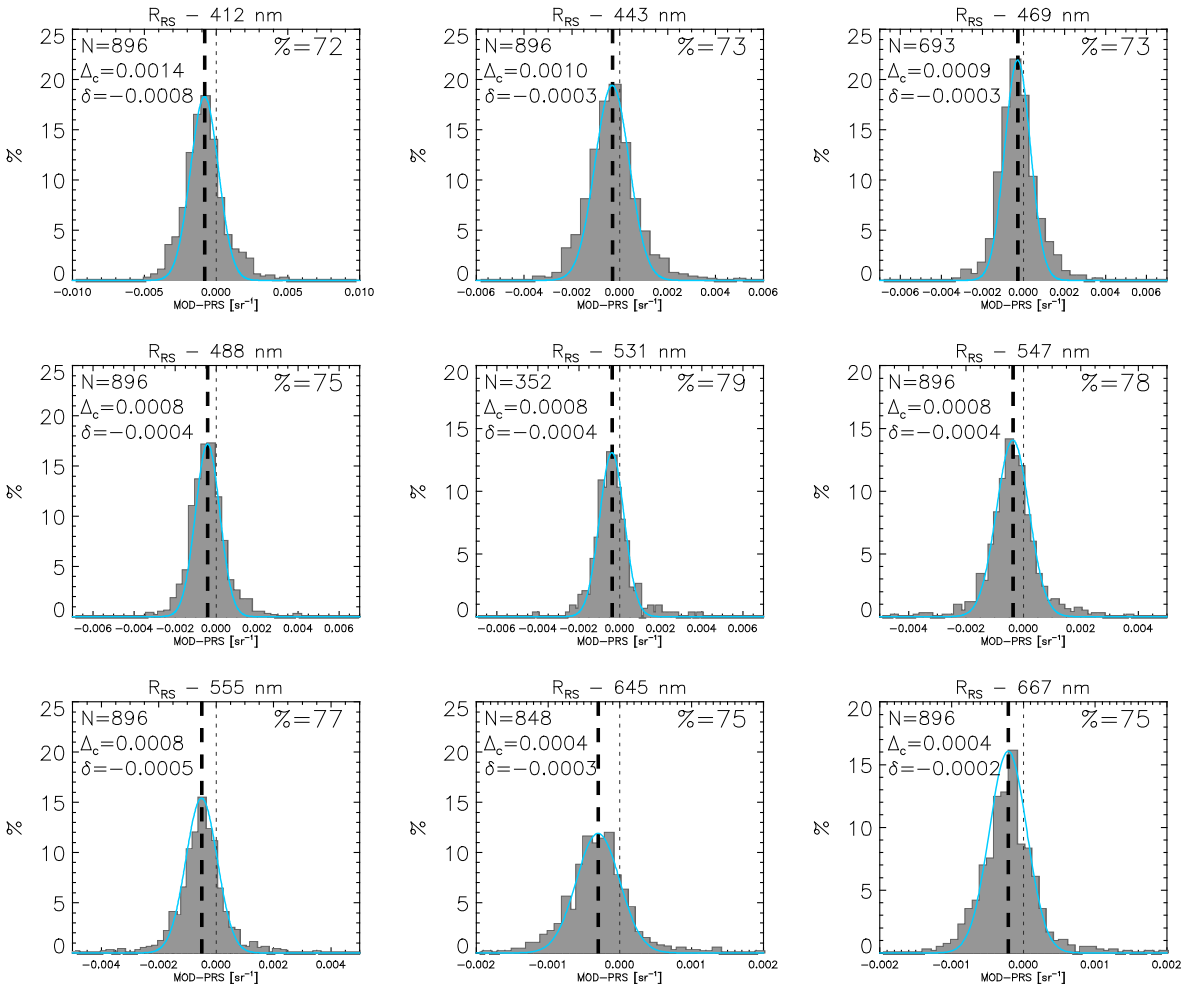

Figure 9. Residuals of the comparison between field and MODIS-A R_{RS} data (see scatter plots in Fig. 6). The blue curves are Gaussian functions of width Δ_c (centered RMS difference) centered at δ (mean difference). '%' gives the percentage of residuals found in the interval $[\delta-\Delta_c; \delta+\Delta_c]$.

3.3 Analysis of Validation Results

This section goes beyond the mere presentation of validation results by conducting some additional analysis allowed by the fairly large number of match-ups available.

The first question addressed here is the extent to which residuals depend on observation conditions. This is a very challenging question as conditions associated with the water content, atmospheric properties (particularly the aerosols) or the conditions of illumination all vary with their own time scales, and it is hard to distinguish the impact of one factor independently from others. For instance, average Sun elevation varies smoothly during the year but it is not straightforward to analyse its impact on the retrievals as atmospheric and water constituents also have a seasonal cycle.

Just 2 representative examples are given hereafter. Fig. 10 shows the evolution of residuals (in sr^{-1}) as a function of the air-mass ($1/\cos\theta+1/\cos\theta_0$, where θ and θ_0 are satellite and Sun zenith angles, respectively) for the case of MODIS-A residuals at the AAOT site (443 nm). For this analysis, the flags marking high zenith angles are not activated. Residuals appear to be fairly stable, increasing towards positive values only for air mass higher than 3.5 (part of these cases being flagged in a standard processing).

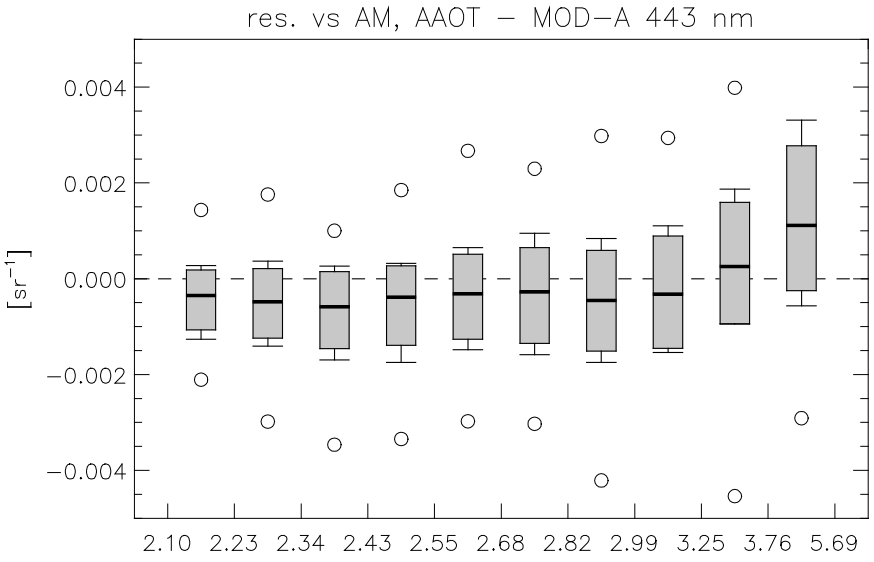

Figure 10. Whisker plots (median, standard deviation, 10th and 90th percentile, minimum/maximum) for the MODIS-Aqua residuals, binned by value of air-mass at AAOT (bins contain the same number of match-ups).

Another example in Fig. 11 shows the dependence of MODIS-A residuals (at 547 nm) at GLR on the Ångström exponent. There is no significant variation of the residuals as a function of this aerosol parameter.

Other analyses as a function of sun and satellite zenith angles, aerosol optical depth, chlorophyll-a concentration (as computed using AERONET-OC data), time difference between field data and satellite overpass, or coefficient of variation , do not generally show much of variations (for a given site), suggesting that the atmospheric correction is fairly robust, at least in its domain of applicability.

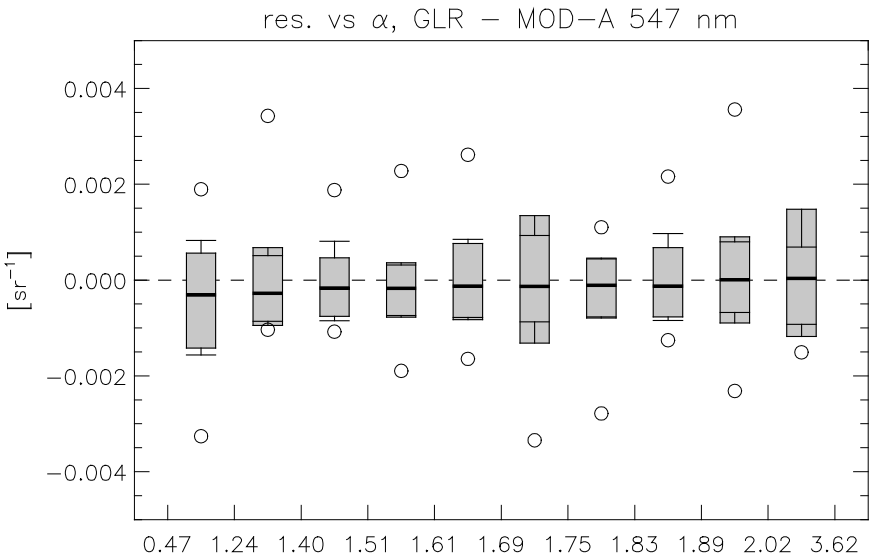

Figure 11. Whisker plots (median, standard deviation, 10th and 90th percentile, minimum/maximum) for the MODIS-Aqua residuals, binned by value of Ångström exponent at GLR (bins contain the same number of match-ups).

r	412	443	469	488	531	547	555	645	667
412		0.92	0.81	0.76	0.56	0.41	0.39	0.21	0.26
443	0.93		0.90	0.85	0.68	0.52	0.48	0.32	0.36
469	0.83	0.93		0.94	0.81	0.66	0.60	0.43	0.53
488	0.80	0.90	0.97		0.86	0.75	0.68	0.50	0.59
531	0.67	0.79	0.87	0.90		0.85	0.86	0.70	0.79
547	0.60	0.71	0.79	0.84	0.90		0.97	0.80	0.83
555	0.59	0.69	0.77	0.82	0.90	0.99		0.82	0.79
645	0.56	0.64	0.71	0.74	0.78	0.80	0.77		0.88
667	0.56	0.64	0.71	0.74	0.76	0.77	0.73	0.97	

Table 1. Spectral cross-correlation between residuals for MODIS-A at AAOT (left/lower part of the table) and HLT (right/higher part).

Another question addressed here is the correlation between residuals across the spectrum. It is known that R_{RS} values are well correlated from one wavelength to a neighbour wavelength but this does not mean that residuals would follow this behaviour. Table 1 suggests a fairly strong correlation between residuals (example of MODIS-A data at AAOT and HLT). For instance, residuals between 2 neighbour wavelengths (diagonals just off the main diagonal) are all related by a correlation coefficient larger than 0.77 (often larger than 0.9). Some of the MODIS bands (469, 555, 645 nm) were originally intended for land and atmospheric applications and have lower signal-to-noise ratios than the ocean colour bands; nevertheless correlations hold for these bands as well. As expected, the

correlation coefficients decrease when the wavelengths are more distant. For instance, residuals at 412 and 645 nm are correlated with r as low as 0.21 at HLT, but the lowest correlation obtained for AAOT is 0.56 (between 412 nm and 645/667 nm). These fairly high levels of correlation show that the residuals are not randomly distributed across the spectrum and indicate the signature of an imperfect atmospheric correction: as the aerosol model selected by the algorithm differs from the actual aerosol conditions, a certain shape of the residual is found and the fact that high correlation coefficients are observed suggests that this effect follows some recurrent patterns.

The last point analysed is the correlation between residuals for different missions. Specifically, match-ups obtained for the same day for a pair of missions are isolated and the correlation coefficient between residuals for similar wavelengths are computed (Fig. 12). At AAOT (Fig. 12a), all correlation coefficients are above 0.5 except for the green and red bands between SeaWiFS and MODIS-Terra. This exception is actually not seen at the GDLT site where the correlation for this pair of missions is the highest (above 0.8 except at 443 nm, 0.66). At GDLT, the pair with the lowest correlation is MODIS-Terra and VIIRS, which might be partly explained by the limited number of match-ups (22). Similar results are found for other sites. For instance, correlations are found between 0.6 and 0.8 at GLR (Black sea) for all 3 pairs associated with 3 available missions (MODIS-Aqua, MODIS-Terra, VIIRS). It is important to recall that the algorithm is the same for all missions considered here, and these results suggest that, in the conditions encountered for a given day, the algorithm behaves in a similar way, regardless of the mission.

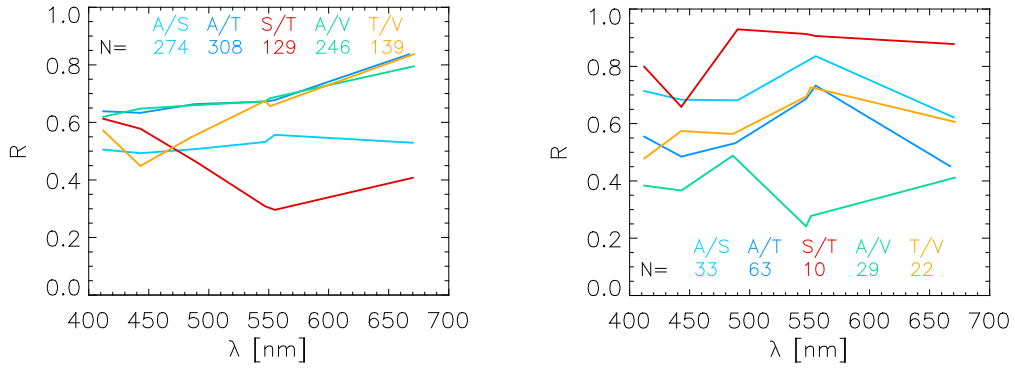

Figure 12. Correlation coefficients between residuals obtained for pairs of missions at similar wavelengths (e.g., VIIRS 410 vs MODIS 412). The number of pairs of match-ups are listed. Examples shown here are for a) AAOT and b) GDLT.

4 Impact of Adjacency Effects in Coastal Data Products [3]

Standard algorithms for the processing of OC satellite data generally assume an infinite water surface, thus neglecting the presence of land in coastal waters. As a consequence, the radiance reflected by the land and then scattered by the atmosphere in the field of view of the sensor becomes a source of spectral perturbations, leading to uncertainties in derived primary products. Such a phenomenon is called *adjacency effects* (AE).

With specific reference to satellite observations of coastal regions, this section summarizes most recent theoretical analysis and quantifications of adjacency perturbations by building on the long-standing experience of the JRC in the modelling of OC satellite and *in situ* observations.

Uncertainties in OC products can be efficiently investigated through accurate radiative transfer modelling (RTMs), able to theoretically reconstruct the different components of the signal at the sensor by accounting for any possible interaction of the solar radiation with the optically active components of the system. Accurate and efficient modelling capabilities in turn rely on i) accurate radiative transfer algorithms, mathematically describing the propagation of the radiance through a defined system, and ii) an accurate optical characterization of the medium in which the radiance propagates. It is clear that the latter highly benefits from extensive and accurate *in situ* measurements of the inherent (IOPs) and apparent (AOPs) optical properties of the system. It is decisively essential the synergetic use of robust and efficient radiative transfer algorithms in combination with accurate *in situ* measurements, which allow the greatest modelling capabilities.

In-house modelling capabilities (i.e., the Advanced Radiative Transfer Models for In-situ and Satellite Ocean Colour data, ARTEMIS-OC) comprise highly accurate RTMs for the propagation of the solar radiation in the atmosphere-ocean system, namely: a plane-parallel numerical code based on the Finite Element method for the simulation of OC satellite data (FEMRAD-OC) [Bulgarelli et al., 1999] and the Novel Adjacency Perturbation Simulator for Coastal Areas (NAUSICAA) full three-dimensional (3D) backward Monte Carlo code [Bulgarelli et al., 2014].

4.1 Simulation of Adjacency Effects

AE are quantified in terms of *adjacency radiance* L_{adj}, defined as the difference in the radiance at the sensor between the case accounting for the non-uniformity of the underlying reflecting surface and the case assuming a uniform surface. As such, L_{adj} can range from negative to positive values.

The adjacency radiance L_{adj} and its percent contribution to the total radiance at the sensor L_{tot} have been simulated assuming a stratified atmosphere (modeling the vertical distribution of gas molecules and aerosols) bounded by a reflecting surface, and fully accounting for multiple scattering, sea surface roughness, slanted illumination and observation conditions. NAUSICAA simulations additionally include a non-uniform reflecting surface accounting for coastal morphology.

In order to reduce computing time in MC simulations, L_{adj} has been parameterized as [see Bulgarelli et al., 2014 and 2018c for details]:

$$L_{adj} = \{\rho_I \cdot \kappa_I - R_{rs} \cdot \kappa_w\} \cdot C^{\rho=1} - W \ ,$$

where the albedo of the land ρ_I and the remote sensing reflectance R_{RS} have been both assumed isotropic and spatially homogeneous; the functions $C^{\rho=1}$ and W designate the cumulative radiance contribution at the sensor originating from the land assumed as an ideal Lambertian reflector and as a Fresnel wind-roughened sea surface, respectively; and parameters κ_I and κ_w are scaling factors to adjust the radiance reflected by an ideal Lambertian reflector to that reflected by an actual land surface and to that leaving the water volume, respectively. The term W is often called the *Fresnel mask*.

[3] This section summarizes finding from Bulgarelli and Zibordi (2018).

The proposed modeling allows to decouple land and water optical properties from the atmospheric scattering, while accurately describing the anisotropy of the sea surface [modeled according to Kisselev and Bulgarelli, 2004]. Once the functions $C^{\rho=1}$ and W are computed for given geometric and atmospheric inputs, the basic equation of L_{adj} allows a straightforward evaluation of the AE for a wide variety of land and water spectral signatures. The latter can be extrapolated from satellite-derived or *in situ* measured data.

4.2 Relevance of Adjacency Effects in Satellite Observations

The relevance of AE with respect to the radiometric resolution of the Ocean and Colour Instrument (OLCI) on-board Sentinel-3 and the MultiSpectral Instrument (MSI) on-board Sentinel-2, has been assessed by comparing the percent adjacency contribution at the sensor $\xi_{L_{tot}} = 100 \cdot L_{adj}/L_{tot}$ with the percent noise level NL=100/SNR, opportunely harmonized to the same input radiance typical of cloud-free OC scenes (Bulgarelli et al., 2018b). It is recalled that NL for OLCI acquisitions in reduced resolution (RR) is 1/4 of NL for OLCI acquisitions performed in full resolution (FR).

Any adjacency radiance contribution lower than NL is regarded as not discriminable from noise, i.e., not detectable.

The analysis has been performed for a wide range of test cases well representing typical mid-latitude coastal environments [Bulgarelli et al., 2018b]. Results are depicted in Fig. 13 along a 36 km study transect extending perpendicular to a half-plane of uniform land albedo. As expected, values of $|\bar{\xi}_{L_{tot}}|$ monotonically decrease with the distance from the coast, and their magnitude increases with the spectral albedo of the land cover.

For both OLCI and MSI sensors, mean adjacency contributions in the presence of snow, white sand, concrete and dry vegetation are above NL throughout the considered transect and at all wavelengths. Conversely, adjacency contributions in the presence of green vegetation and bare soil might become lower than sensor NL within the transect, at a distance that increases with the radiometric sensitivity of the sensor. It is hence the longest for OLCI-RR, and the shortest for MSI (apart for λ=443 nm, where largest NL occur for OLCI-FR). As an example, perturbations for green vegetation and brown loam at 555 nm become lower than NL at ~3 km offshore for MSI, ~15 km for OLCI-FR, while they are above the noise thresholds throughout the whole 36 km-transect for OLCI-RR. It is noted that for highly sensitive OLCI-RR acquisitions mean adjacency contributions drop below NL at distance from the coast shorter than 36 km at the sole red center-wavelengths with green vegetation. It is also mentioned that green vegetation and bare soil contributions at blue center-wavelengths are negative.

Different observation geometries, as well as the mutual location of sun, sensor and land, influence actual adjacency contributions (not shown here, see Bulgarelli et al., 2014 and 2018b for details). In specific, results highlight a significant increase of AE with the viewing angle. For slanted observations and when the land reflectance is consistently larger than the sea one (i.e., throughout the spectrum for snow, dry vegetation, white sand and concrete, or at the sole near-infrared (NIR) wavelengths for green vegetation and bare soil) AE are consistently larger when the sensor is observing from over the land. Adjacency perturbations additionally show a significant seasonal variation [Bulgarelli et al., 2018a].

How adjacency perturbations at the sensor propagates into uncertainties in radiometric products strictly depends on the atmospheric correction procedure applied [Bulgarelli et al., 2017].

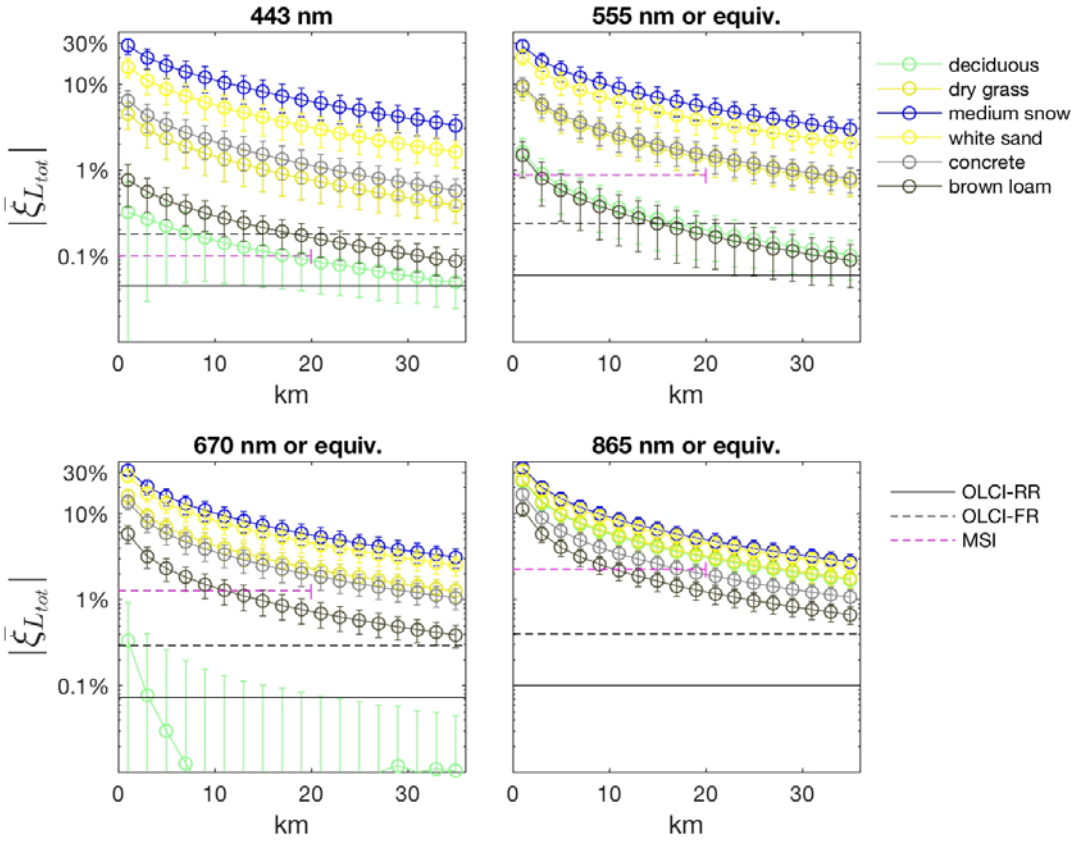

Figure 13. Values of $|\bar{\xi}_{L_{tot}}|$ at representative wavelengths and as a function of the distance from the coast along the study transect. Case-2 moderately sediment-dominated waters [Zibordi et al., 2011] and different land covers [Baldridge et al., 2009] are selected. Error bars represent the standard deviation. Horizontal lines indicate sensors' NL.

Fig. 13 illustrates biases on tL_w (i.e., the water leaving radiance at the sensor, with t representing the atmospheric transmittance) theoretically estimated for a correction scheme determining the atmospheric properties from the NIR region through a power-law spectral extrapolation, as for the single-scattering approximation of the Gordon and Wang correction algorithm [Gordon and Wang, 1994]. Results indicate that AE at NIR wavelengths (affecting the retrieval of the atmospheric radiance) might compensate adjacency perturbations at the visible wavelengths. Consequently, biases on the retrieved water-leaving radiance are not directly correlated to the strength of the land spectral albedo. As an example, the impact of AE on the water signal retrieved at the blue wavelengths might be larger for a vegetation land cover than for the more highly reflective concrete or white sand. Compensations might even occur in the presence of snow. Results from Fig. 14 further indicate that percentage over- and underestimates of the radiance from moderately sediment-dominated waters (e.g., northern Adriatic waters) at the coast might well exceed 100% at 443 nm in the presence of snow and green vegetation, respectively. It is mentioned that misestimates might increase about 4 times for CDOM-dominated waters, like those of the Baltic Sea [Bulgarelli and Zibordi, 2018b].

It is remarked that the retrieval of the atmospheric properties from MSI data is generally performed utilizing one or two short-wave infrared (SWIR) bands (such as those centered around 1600 and 2200 nm [e.g., see Vanhellemont and Ruddick, 2015]). Although the analysis of AE at SWIR wavelengths (where land albedos generally consistently differ from values in the NIR) has not been specifically addressed, it is nonetheless expected that analogous mechanisms of propagation of adjacency perturbations from the SWIR to the visible, as well as potential compensations between adjacency perturbations at SWIR and visible wavelengths, can occur.

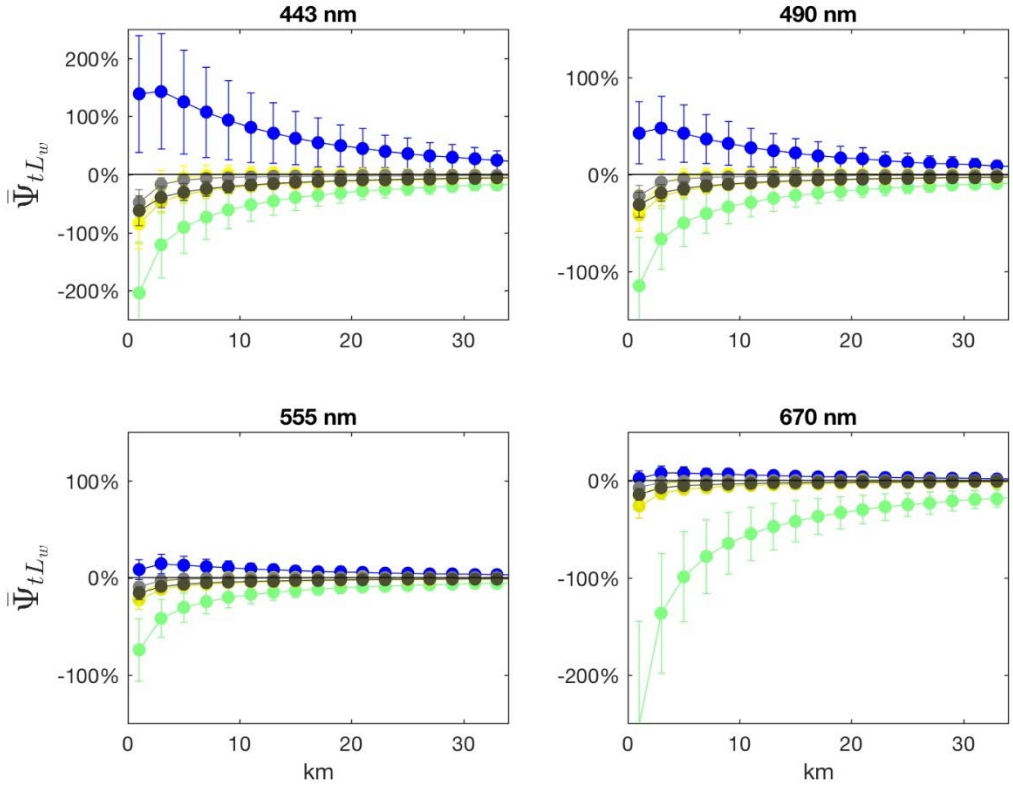

Figure 14. Values of average biases Ψ_{tLw} induced by adjacency perturbations on tL_w when derived with an AC-2 scheme applying a power law extrapolation to derive the aerosol properties from NIR center-wavelengths. Results are given for moderately sediment-dominated waters [Zibordi et al., 2011] and representative land covers (see legend of Fig. 13) as a function of the distance from the coast and at representative center-wavelengths. Error bars indicate ± 1 standard deviation (N = 24 test cases).

Notably, a validation exercise performed with the NASA SeaWiFS Data Analysis System (SeaDAS) on a sample of cloud-free images acquired by the Sea-viewing Wide Field-of-view Sensor (SeaWiFS) at the AAOT site, and alternatively ingesting original SeaWiFS data and SeaWiFS top-of-atmosphere data corrected for estimated adjacency contributions, indicated a significant decrease of annual and intra-annual biases at all wavelengths when correcting for AE [Bulgarelli et al., 2018c].

The same exercise additionally indicated AE at the AAOT larger than the estimated turbid water (TW) contributions in summer and mid-seasons, and hinted the occurrence of a systematic overestimate of the NIR water signal by the TW correction algorithm within the standard SeaDAS procedure, partially compensating for AE.

Notably, compensations of AE within the SeaDAS processing scheme allows explaining why previous analysis at sample validation sites did not provide firm evidence of appreciable AE in satellite primary products [Zibordi et al., 2009].

The validation exercise additionally allowed to explain the intra-annual variation in biases observed in SeaWiFS primary products acquired at the AAOT in the period 2002-2010 [Zibordi et al., 2012] as the likely consequence of residual AE in data acquired in summer, and of misinterpretation of NIR atmospheric signal as TW contributions in data acquired in winter.

4.3 The Adjacency Field Around the Lampedusa Island

The Lampedusa Island (35.52º, 12.57º) located in the southern Mediterranean Sea, is considered for the positioning of a System Vicarious Calibrations (SVC) site for OLCI measurements. Annual average values of $\xi_{L_{tot}}$ in OLCI data over the marine region surrounding the island are illustrated in Fig. 15 at λ=865 nm where AE are spectrally the

highest. Results are for typical observation conditions (i.e., θ_v=20º, ϕ_v=100º, θ_0=48º and ϕ_0=160º, and average land and water optical conditions). Remarkably, the adjacency field shows a significantly different pattern south and north of the island. AE are always positive (up to 37%) in the southern side, while a remarkable influence of the masked sea surface (the term *W* in the equation applied for the determination of L_{adj}) leads to negative AE (up to -1%) in correspondence of the reflected sunbeam in the northern part of the island. Masked sea surface contributions highly depend on the anisotropy of the surface reflectance (i.e., on wind speed and direction) and on the sun position. This hinders the possibility to deliver a general assessment of the impact of AE in the northern marine region. In the remaining water regions, adjacency contributions at 865 nm exceed NL up to ~5-7 km offshore for OLCI-FR, and up to 10-12 km offshore for OLCI-RR.

The analysis further indicates that AE along a representative transect intercepting an existing oceanographic buoy (see Fig. 15) become lower than NL for all observation conditions and at all center-wavelengths with a 99.7% level of confidence (corresponding to 3σ) at ~8 and 14 km for OLCI-FR and OLCI-RR, respectively.

By also considering that SVC relies on the application of a number of images, which may lead to a decrease of NL, still a fully confident avoidance of AE in the indirect calibration of OLCI data might suggest to locate the site even further away from the coast.

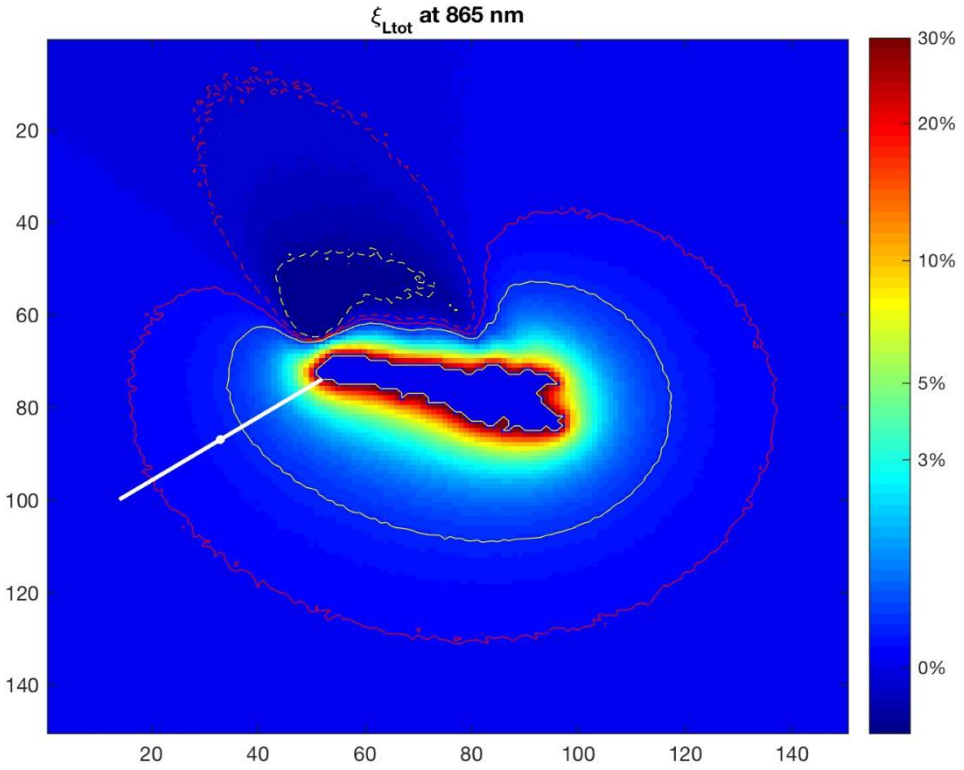

Figure 15. ξ_{Ltot} at 865 nm for θ_v=20º, ϕ_v=100º and average illumination, land and water optical conditions. The white straight line indicates the transect intercepting an existing oceanographic buoy (white dot) and extending up to 13 km offshore. The yellow and red contour lines designate NL for OLCI-FR and OLCI-RR, respectively. Dashed contour lines are for –NL, full contour lines for +NL.

5 Impact of *In Situ* Instruments Characterizations[4]

Differences between values of measured quantities and the true values of measurands are indicated as errors. These may comprise *i*. systematic components indicating biases due to lack of accuracy, and *ii*. random components indicating dispersion due lack of precision. Bias components are generally minimized through corrections.

Uncertainties quantify the incomplete knowledge of the measurand through the available information. Thus, *a measurement of any kind is incomplete unless accompanied with an estimate of the uncertainty associated with that measurement* [JGUM 2008].

Uncertainties are generally classified into type A when determined through statistical methods and type B when determined by means other than statistical (e.g., models, published data, calibration certificates, or even experience). Type A and type B uncertainties can additionally be separated into additive (i.e., independent of the measured value such as the values related to the dark signal) or multiplicative (i.e., dependent on the measured value such as those related to the absolute responsivity of the radiometer). All uncertainties contribute to the overall measurement uncertainty through their combined values. When the various uncertainties are independent, the combined uncertainty can be determined as the quadrature sum (i.e., the root square sum) of the various contributions. The level of confidence of each uncertainty, defined by the coverage factor k, should be provided with the uncertainty estimate. Standard uncertainties refer to a confidence level of 68% determined by $k = 1$, while expanded uncertainties defined by $k>1$ refer to confidence levels of approximately 95% ($k\approx2$) or 99% ($k\approx3$).

Uncertainties, when possible, should be provided in both relative (i.e., %) and physical units. The range of values for which the uncertainties are proposed should also be reported together with details on measurement conditions. In fact, uncertainties determined for a specific range of values may not necessarily be the same for other ranges or different measurement conditions.

5.1 Uncertainty Requirements

The quantification of uncertainties of *in situ* radiometric measurements, should comprehensively address contributions from the calibration source and its transfer, the performance of the radiometer and of any model applied for data reduction, effects of environmental variability, and perturbations by the instrument housing and deployment platform.

An uncertainty threshold of 5% was originally defined for satellite derived $L_{WN}(\lambda)$ in the blue spectral region to restrict to within 35% the uncertainties in chlorophyll-*a* concentrations determined in oligotrophic waters with existing bio-optical algorithms [Gordon and Clark 1981]. This 5% uncertainty threshold was then set as the target for $L_{WN}(\lambda)$ determined from the major ocean colour missions. The maximum uncertainty values given for $L_{WN}(\lambda)$ unavoidably prompt the need for uncertainties better than 5% for *in situ* optical radiometry data.

5.2 Uncertainty Estimate for *In Situ* L_w

Table 1, filled using accessible information from various literature sources, provides a basic example of uncertainty budget produced for $L_W(\lambda)$ data determined from sub-surface hyperspectral radiometric measurements. Neglecting uncertainty contributions due to instrumental performance such as temperature dependence, non-linearity, stray light, polarization sensitivity and also ignoring avoidable contributions to instrument deployment such as tilt assuming these are minimized by an aggressive filtering of data, Table 1 summarizes spectral uncertainty contributions $u_i(\lambda)$ at the 443, 555 and 665 nm center-wavelengths as resulting from: *i.* uncertainty of the absolute calibration of the L_u sensor accounting for specific contributions from an FEL lamp irradiance standard, reflectance plaque, and mechanical positioning of the various components [Hooker *et al*. 2002]; *ii*.

(4) This section summarizes finding from Zibordi and Voss (2014) and Zibordi (2018).

uncertainty due to the experimental determination of the immersion factor [Zibordi and Darecki 2006]; *iii.* uncertainty of the correction factors applied for removing self-shading perturbations computed as 25% of the corrections applied to a 5 cm diameter radiometer with 1 cm aperture.

In agreement with metrology principles, the combined spectral uncertainties $u(\lambda)$ are given by the quadrature sum of the uncertainty contribution $u_i(\lambda)$ assumed independent from each other, according to

$$u(\lambda) = \sqrt{\left[u_1(\lambda)\right]^2 + \left[u_2(\lambda)\right]^2 + ... + \left[u_n(\lambda)\right]^2} \ .$$

The combined relative uncertainties $u(\lambda)$ in Table 1 are in the range of 3-4% for the selected spectral bands (see the left values in the various columns presenting data at 443, 555 and 665 nm).

However, often field measurements are affected by unpredictable errors because of the lack of radiometers characterization. Benefitting of comprehensive characterizations of RAMSES (TriOS, Rastede, Germany) hyperspectral radiometers, it is hereafter evaluated the impact of systematic errors affecting field measurements. Specifically, the values in red shown in the right of each column of Table 2, indicate expected spectral errors $\varepsilon_m(\lambda)$. The resulting combined spectral uncertainties $u(\lambda)$ are then computed as

$$u(\lambda) = \sqrt{\left[\varepsilon_1(\lambda) + \varepsilon_2(\lambda) + ... + \varepsilon_m(\lambda)\right]^2 + \left[u_1(\lambda)\right]^2 + \left[u_2(\lambda)\right]^2 + ... + \left[u_n(\lambda)\right]^2} \ .$$

Table 2. Combined spectral uncertainties $u(\lambda)$ (in percent) of L_w determined from sub-surface data.

Uncertainty source	*443*		*555*		*665*	
Absolute calibration	2.7	2.7	2.7	2.7	2.7	2.7
Immersion factor	0.2	-0.6	0.2	-0.9	0.2	-1.2
Temperature response (+5C)		+0.2		-0.3		-0.7
Polarization sensitivity		+0.1		+0.2		+0.4
Stray-light effects		-1.0		+0.5		+0.5
Nonlinearity		-0.0		-1.0		-0.2
Self-shading correction	0.3	-1.2	0.1	-0.8	0.8	-3.2
Environmental effects	2.1	2.1	2.2	2.2	3.2	3.2
Combined	3.4	4.2	3.5	4.2	4.3	6.1

As expected, biases due to errors may lead to an increase of the combined uncertainties. Still, the preservation of the sign of $\varepsilon_m(\lambda)$ in the determination of combined uncertainties $u(\lambda)$, explains compensations that may mask the impact of individual error sources. This clarifies the apparent equivalence of matchup analysis relying on extensive efforts to minimize sources of uncertainties and those analysis applying plain data from field instruments. Still, data in Table 1 indicate that compensations processes due to systematic errors may vary as a function of wavelength and measurement conditions, and consequently lead to unpredictable spectral impacts.

The above results developed for the very basic case of sub-surface L_W measurements would be much enhanced in the case of more complex measurement protocols relying on the use of data from multiple radiometers. This finding further and quantitatively confirms the fundamental need for comprehensive radiometric calibrations and characterizations of radiometers devoted to the production of validation measurements.

6 Reproducibility of Laboratory Pigments Analysis[5]

The validation of satellite data products requires availability of high quality *in-situ* measurements of chlorophyll *a* (TChl *a*, often simply indicated as *Chla*) and phytoplankton pigments. High Pressure Liquid Chromatography (HPLC) is the method of choice for the quantification of photosynthetic pigments and it is routinely used for phytoplankton pigment analysis [U.S. JGOFS Protocols, 1991].

An upper uncertainty of 25% for the TChl *a* is deemed acceptable for validation purposes[Hooker and McClain, 2000]. In the last 18 years, several round robin and inter-comparison exercises were performed to assess the performance of HPLC methods applied for the determination of phytoplankton pigments. During SeaWiFS HPLC Analysis Round-Robin Experiments [SeaHARRE, Hooker et al. 2010] and the HPLC Inter-comparison of Pigments [HIP, Canuti et al., 2016] a 15 % uncertainty was achieved for TChl *a* and several other pigments.

From 2012 till 2017, an additional uncertainty analysis has been performed benefitting of duplicate samples separately analysed by two quality-certified laboratories that already showed a good performance in previous inter-comparisons. This new exercise relied on 961 phytoplankton pigment samples collected during 11 oceanographic cruises (OC) performed across European seas, including the Black Sea, the Eastern Mediterranean Sea, the Iberian Shelf in the Atlantic waters, and additionally 26 campaigns carried out at the AAOT in the northern Adriatic Sea. The samples are representative of different trophic conditions with TChl *a* concentration varying in the range of 0.083 - 27.35 µg/L. The laboratories involved in the comparison are the Joint Research Center of the European Commission (*J*) and the Danish DHI Institute for Water and Environment (*D*). JRC is Quality Standard ISO 9001 certified, while DHI is DANAK quality accredited (ISO/IEC 17025:2005) for phytoplankton analysis. The quantitative HPLC - Diode Array Detector (HPLC–DAD) method applied by the two laboratories for the determination of phytoplankton pigments is that detailed by Van Heukelem and Thomas [2001]. It is mentioned that this method has been successfully applied to a wide range of pigment concentrations including the oligotrophic central South Pacific Ocean waters analyzed during SeaHARRE-3 and the eutrophic coastal South African waters included in SeaHARRE-2. Both *D* and *J* laboratories participated in SeaHARRE [Hooker et al., 2010] and HIP inter-comparisons [Canuti et al., 2016].

The natural water pigments matter of the laboratory inter-comparisons are chlorophylls and carotenoids most commonly used in chemotaxonomic and photophysiological studies. These are classified as primary and ancillary (*i.e.*, secondary and tertiary pigments), as established by the Scientific Committee on Oceanographic Research (SCOR) [Jeffrey et al. 1997]. The inter-comparisons have also been extended to the higher-order variables formed by sums and ratios of pigments concentrations commonly applied in the development of bio-optical algorithms (see Table 3).

Table 3. Pigment Sum compositions

Pigment Sum	Individual Pigments
TChl a	Total Chlorophyll a (Chlide a + DV Chl a + Chla a)
TChl	Total Chlorophyll (TChl a + TChl b + TChl c)
PPC	Photoprotective Carotenoids (Allo + Diad + Diato + Zea + Caro)
PSC	Photosyntetic Carotenoids (But + Fuco + Hex + Peri)
PSP	Photosynthetic Pigments (PSC + TChl)
TAcc	Total Accessory Pigment (PPC + PSC +TChl b + TChl c)
TPig	Total Pigment (TAcc + TChl a)
DP	Total Diagnostic Pigment (PSC +Allo +Zea + TChl b)

(5) This section summarizes finding from Canuti (2018).

6.1 Statistical Evaluation

The limit of agreement between *J* and *D* laboratories is determined assuming the differences between the data from the two laboratories are normally distributed and the standard deviation and the mean are the same across all the range of measurements. The differences between the concentrations of the *N* sample analyses produced by the laboratories *J* and *D*, has been quantified through relative percent differences ($\psi_{i,p}$) against the average of the inter-laboratory values for each sample *i* and pigment *p* according to

$$\psi_{i,p} = 200\,\frac{C_{i,p}^{J} - C_{i,p}^{D}}{C_{i,p}^{J} + C_{i,p}^{D}},$$

and adopting the standard deviation s_p of the $\psi_{i,p}$ values as an error index

$$s_p = \sqrt{\frac{\sum_s^N (\psi_{i,p} - \overline{\psi_p})^2}{N-1}}$$

with $\overline{\psi_p}$ indicating the mean of the $\psi_{i,p}$ values.

6.2 Results

The analysis of pigments concentrations performed on duplicate samples by the two laboratories is here after summarized for the different Pigment Sums compositions. Result exhibit high correlations across a wide range of concentrations of TChl *a* (i.e., 0.08 - 27.35 µg/L) with the highest values (R^2≥0.93) occurring for TChl *a*, Total Carotenes (α Carotene + β Carotene), Diadinoxanthin, Fucoxanthin, and all the Pigment Sums presented in Fig. 16.

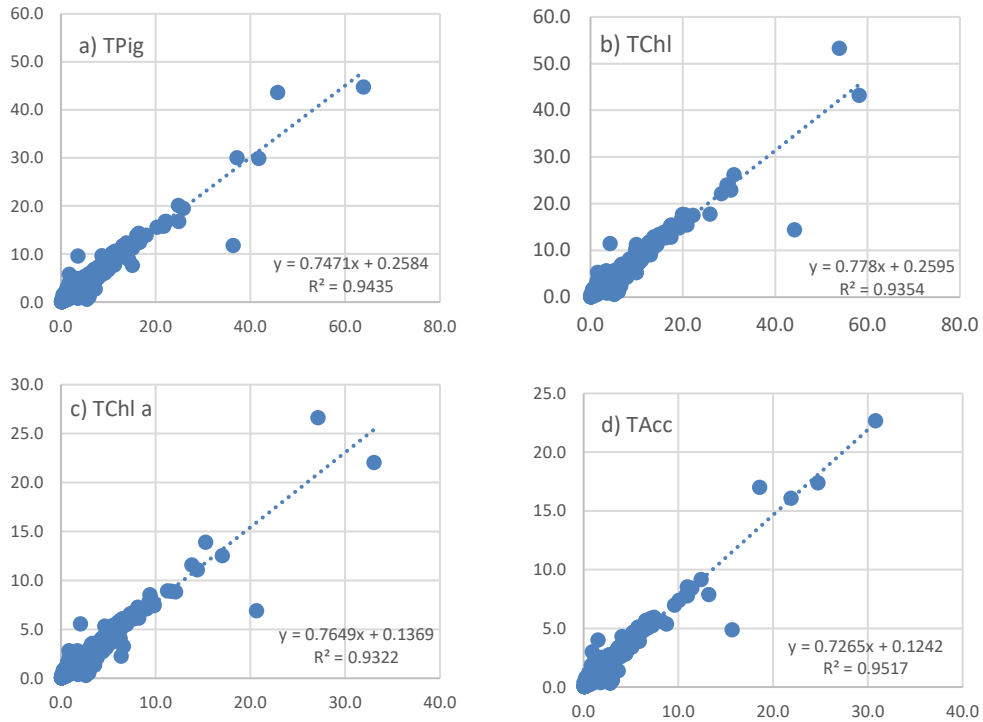

Fig. 16. Scatter plots of concentrations in µg/L determined from the *J* and *D* laboratories for **a)** Total Pigments (TPig), **b)** Total Chlorophylls (TChl), **c)** TChl *a* for the Primary Pigments and **d)** Total Accessory Pigments (TAcc). The trend line and regression coefficient are shown in each plot.

As expected, results indicate a decrease in correlation for pigments usually detected at low concentration (*e.g.,* 19'-Butanoyloxyfucoxanthin and Zeaxanthin) and pigments often characterized by values close to the Low Limit of Detection, which may lead to false biases. Notable, a mean difference of 10.8% (i.e., the mean of the relative values of $\psi_{i,p}$) with standard deviation s_p of 22.7% (largely explained by the inhomogeneity of duplicate samples), has been determined for the two independent set of laboratory analyses of TChl *a*. This result suggests the capability of both JRC and DHI to satisfy the general requirement of 25% uncertainty associated with TChl *a* pigments determinations for the validation of satellite data products [Hooker and McClain, 2000].

7 Conclusions

This Report aims at summarizing findings from a number of recent JRC investigations constituting a comprehensive asset to continuously address the fitness-for-purpose of Copernicus ocean colour data products. These investigations embrace:

- The accuracy of radiometry data from the Ocean and Land Colour Instrument (OLCI) on board Sentinel-3a, addressed relying on geographically distributed *in situ* reference measurements from autonomous systems and dedicated oceanographic campaigns.
- Uncertainties of ocean colours radiometry data from a number of international missions, to evaluate the potentials for the construction of Climate Data Records (CDRs) from independent missions.
- The impact of adjacency effects in coastal data limiting the accuracy of ocean colour radiometry products, addressed by relying on state-of-the-art radiative transfer simulations to quantify adjacency effects in space data from sensors exhibiting different signal to noise ratios.
- Uncertainties affecting *in situ* radiometry data for the validation of satellite data products in the absence of comprehensive characterizations of field instruments.
- Reproducibility of the experimental determination of pigments concentrations for the validation of satellite data products, addressed through differences between pigments concentrations determined with equivalent methods by different laboratories.

The following main conclusions are hereafter summarized:

- The comparisons between OLCI and *in situ* normalized water-leaving radiances L_{WN} indicate systematic underestimates of satellite radiometric products, with effects more pronounced in the blue and red spectral regions. These are likely explained by the difficulty to separate water and atmospheric contributions due to biases in calibration coefficients or a low performance of the Bright Pixel Correction (BPC), which results in a poor determination of aerosol load and type, and a consequent systematic overestimate of atmospheric effects.
- The analysis of validation results across different ocean colour missions and *in situ* reference sites, indicate that the spectrum of RMS differences between satellite and field values of remote sensing reflectance R_{rs} most often shows a decrease with wavelength, with values in the blue generally between 0.0008 and 0.0025 sr^{-1}. Usually, the distribution of differences shows an approximately normal shape, which allows a statistical interpretation of the associated RMS differences. Average relative differences (in %) display a large variability, with values nearing 10% in the middle range of wavelengths and increasing in a typical horseshoe shape towards the blue and red bands. Validation statistics tend to vary more across sites than across missions. In fact, results are often very similar for different missions at a given site. The atmospheric correction used for the considered missions appears fairly robust, with some few exceptions, with respect to environmental conditions of retrieval. Interestingly differences appear to be well correlated across the spectrum for a given mission and a given site. Furthermore, using match-ups common to several missions, differences appear significantly correlated across missions (for similar wavelengths), implying that a large part of the differences is not random but associated with the atmospheric correction algorithm. This common behaviour favours the merging of data from different missions, under the strong proviso that the inter-mission bias is small or corrected, and differences with respect to field data could be further reduced with improved atmospheric correction algorithms.

- The analysis of adjacency effects (AE) in satellite ocean colour clearly indicates that their impact depends on the atmospheric correction procedure applied. Specifically, when considering atmospheric corrections relying on the determination of aerosol information from the NIR wavelengths, biases affecting the retrieved water-leaving radiance as a result of AE are not directly correlated to the strength of the land spectral albedo. Further, corrections embedded in atmospheric corrections codes to account for the non-negligible water-leaving radiance in the NIR, may lead to a compensation of AE. Notable, AE effects may exhibit a seasonal dependence that affects validation exercises performed in coastal regions. Finally, adjacency effects may be appreciable also in the surround of relatively small islands, thus suggesting care in the choice of the distance of SVC sites from the coast.
- The lack of a comprehensive radiometric characterization of field radiometers may lead to errors naturally increasing the combined uncertainties of measurements. Still, the preservation of sign of individual errors contributing to combined uncertainties, may lead to compensations that may mask the impact of individual error sources. This clarifies the apparent equivalence of matchup analysis performed by relying on extensive efforts to minimize sources of uncertainties and conversely, those analysis applying plain data from field instruments. Still, compensations processes due to systematic errors may vary as a function of wavelength and measurement conditions, and consequently lead to unpredictable spectral impacts. It is thus fundamental that radiometers devoted to the production of validation measurements undergo comprehensive radiometric calibrations and characterizations.
- Results from the analysis of almost 1000 natural samples of marine water independently processed by two laboratories (i.e., JRC and DHI) indicate a mean difference of 10.8% between total chlorophyll a concentrations. This finding further confirms the capability of both laboratories to satisfy the requirement of 25% uncertainty associated with TChl *a* pigments determinations for the validation of satellite data products.

References

A. M. Baldridge, S. J. Hook, C. I. Grove, and G. Rivera, “The ASTER spectral library version 2.0,”*Remote Sensing of Environment*, 113, 711–715. 2009.

B. Bulgarelli, V. Kisselev, and L. Roberti, “Radiative transfer in the atmosphere-ocean system: the finite-element method,” *Applied Optics,* 38, 1530–1542, 1999.

B. Bulgarelli, V. Kiselev, and G. Zibordi, “Simulation and analysis of adjacency effects in coastal waters: a case study,” *Applied Optics, 53*, 1523-1545, 2014

B. Bulgarelli, V. Kiselev, and G. Zibordi, “Adjacency effects in satellite radiometric products from coastal waters: a theoretical analysis for the northern Adriatic Sea,” *Applied Optics*, *56*, 854–869, 2017

B. Bulgarelli, and G. Zibordi, “Seasonal Impact of Adjacency Effects on Ocean Colour Radiometry at the AAOT Validation Site,” *Geoscience and Remote Sensing Letters, IEEE*, *15*, 488–492, 2018a

B. Bulgarelli, and G. Zibordi, “On the detectability of adjacency effects in ocean colour remote sensing of mid-latitude coastal environments by SeaWiFS, MODIS-A, MERIS, OLCI, OLI and MSI,” *Remote Sensing of Environment*, *209*, 423–438, 2018b

B. Bulgarelli, and G. Zibordi, and F. Melin, “On the minimization of adjacency effects in SeaWiFS primary data products from coastal areas,” *Optics Express*, 26, A709-A728, 2018c

B. Bulgarelli and G. Zibordi, “Analysis of Adjacency Effects for Copernicus Ocean Colour Missions”, EUR 23950 EN, Publications Office of the European Union, Luxemburg, ISBN 978-92-79-93671-5, doi: 10.2760/43628, JRC112829, 2018.

E. Canuti, J. Ras, M. Grung, R. Röttgers, P. Costa Goela, F. Artuso, D. Cataldi, “HPLC/DAD Intercomparison on Phytoplankton Pigments: HIP-1, HIP-2, HIP-3 and HIP-4” *EUR - Scientific and Technical Research Reports*, Publications Office of the European Union JRC104601, 2016.

E. Canuti, “HPLC-DAD Analysis of Phytoplankton Pigments: An Inter-laboratory Comparison” *EUR - Scientific and Technical Research Reports*, Publications Office of the European Union (in preparation), 2019.

EUMETSAT, “Sentinel-3A Product Notice – OLCI Level-2 Ocean Colour Operational Products and Full-Mission Reprocessed Time Series,” Product notice EUM/OPS-SEN3/DOC/17/964713, 2018.

EUMETSAT, “Sentinel-3 OLCI Marine User Handbook,” EUM/OPS-SEN3/MAN/17/907205, 2018.

B. Franz, S.W. Bailey, P.J. Werdell, C.R. McClain, “Sensor-independent approach to the vicarious calibration of satellite ocean colour radiometry,” *Applied Optics*, 46, 5068-5082, 2007.

M. Gergely, M. and G. Zibordi, “Assessment of AERONET-OC L_{WN} uncertainties,” *Metrologia*, 51, 40–47, 2014.

H. R. Gordon and D. K Clark, “Clear water radiances for atmospheric correction of coastal zone colour scanner imagery,” *Applied Optics*, 20, 4175-4180, 1981.

H.R. Gordon and M. Wang, “Retrieval of water-leaving radiance and aerosol optical thickness over the oceans with SeaWiFS: a preliminary algorithm,”*Applied Optics*, 33, 443-452, 1994.

S. B. Hooker and C. McClain, “The calibration and validation of SeaWiFS data,” *Progress in Oceanography*, 45, 427-465, 2000.

S.B. Hooker, C.S. Thomas, L. Van Heukelem, L. Schluter, J. Ras, H. Claustre, M.E. Russ, L. Clementson, E. Canuti, J-F. Berthon, J. Perl, C. Normandeau, J. Cullen, M. Kienast and J.L. Pickney , “The Forth SeaWiFS HPLC Analysis Round-Robin Experiment (SeaHARRE-4)”. NASA Tech. Memo. 2010-215857, NASA Goddard Space Flight Center, Greenbelt, Maryland, 74 pp, 2010.

JGOFS, “Protocols for the Joint Global Ocean Flux Study (JGOFS) Core Measurements,” IOC Manuals and Guides, No. 29. UNESCO, Paris, France: UNESCO Publishing, pp.91-96, 1994.

Joint Committee for Guides in Metrology (JCGM), *Evaluation of Measurement Data—Guide to the Expression of Uncertainty in Measurement (GUM),* JCGM 100:2008, 2008.

V. Kisselev and B. Bulgarelli, “Reflection of light from a rough water surface in numerical methods for solving the radiative transfer equation,” *Journal of Quantum Spectroscopy and Radiative Transfer* 85, 419–435, 2004

F. Mélin, and G. Zibordi, “Validation of satellite radiometric products from multiple missions: Synthesis and analysis” *Ocean Optics XXIV*, Dubrovnik, Croatia, 7-12 Oct. 2018.

F. Mélin, and G. Sclep, “Band shifting for ocean colour multi-spectral reflectance data,” *Optics Express*, 23, 2262-2279, 2015

F. Mélin, G. Zibordi, J.-F. Berthon, S. Bailey, B. Franz, K. Voss, S. Flora, and M. Grant, M., “Assessment of MERIS reflectance data as processed by SeaDAS over the European Seas,” *Optics* Express, 19, 25657-25671, 2011.

F. Mélin, G. Zibordi, T. Carlund, B. N. Holben, and S. Stefan, “Validation of SeaWiFS and MODIS Aqua/Terra aerosol products in coastal regions of European marginal seas,” *Oceanologia*, 55, 27–51, 2013.

F. Mélin, M. Clerici, G. Zibordi, B. N. Holben, and A. Smirnov, "Validation of SeaWiFS and MODIS aerosol products with globally distributed AERONET data," *Remote Sensing of Environment*, 114, 230-250, 2010.

R. F. C. Mantoura, S. W. Wrigh, S. W. Jeffrey, R. G. Barlow, D. E. Cummings, “Filtration and storage of pigments from microalgae, [in:] Phytoplanktonpigments in oceanography: guidelines to modern methods”, S.W. Jeffrey,R. F.C. Mantoura & S.W. Wright (eds.), UNESCO Publ. No 10, Paris, 283–305, 1997.

A.Morel, D. Antoine, and B. Gentili, “Bidirectional reflectance of oceanic waters: accounting for Raman emission and varying particle scattering phase function,” *Applied Optics*, *41*, 6289-6306, 2002.

G. Thuillier, M. Hersé, D. Labs, T. Foujols, W. Peetermans, Gillotay, P.C. Simon, and H. Mandel, “The solar spectral irradiance from 200 to 2400 nm as measured by the SOLSPEC spectrometer from the Atlas and Eureca missions,” *Solar Phys*ics 214, 1–22, 2003.

Q. Vanhellemont and K. Ruddick, “Advantages of high quality SWIR bands for ocean colour processing: Examples from Landsat-8”. *Remote Sensing of Environment*, *161*(C), 89–106, 2015

L. Van Heukelem and C.S. Thomas, “Computer-assisted high-performance liquid chromatography method development with applications to the isolation and analysis of phytoplankton pigments” *Journal of Chromatography* A, 910, 31–49, 2001.

G. Zibordi, “Characterization of Hyperspectral Radiometers, Fiducial Reference Measurements for Satellite Ocean Colour Workshop,” National Physical Laboratory, London October 4-5, 2018.

G. Zibordi, J. F. Berthon, F. Mélin, D. D'Alimonte, and S. Kaitala, “Validation of satellite ocean colour primary products at optically complex coastal sites: Northern Adriatic Sea, Northern Baltic Proper and Gulf of Finland,” *Remote Sensing of Environment*, 113, 2574-2591, 2009.

G. Zibordi, G. and M. Darecki, “Immersion factors for the RAMSES series of hyper-spectral underwater radiometers,” *Journal of Optics A: Pure and Applied Optics*, *8*, 252-258, 2006.

G. Zibordi, F. Mélin, J.-F. Berthon, “A regional assessment of OLCI data products,” *IEEE Geoscience and Remote Sensing Letters*, 15, 1490–1494, 2018.

G. Zibordi, J.-F. Berthon, F. Mélin, and D. D’Alimonte, “Cross site consistent *in situ* measurements for satellite ocean colour applications: The BiOMaP radiometric dataset,” *Remote Sensing of Environment*, 115, 2104–2115, 2011.

G. Zibordi, J. F. Berthon, F. Mélin, D. D'Alimonte, and S. Kaitala, “Validation of satellite ocean colour primary products at optically complex coastal sites: Northern Adriatic Sea, Northern Baltic Proper and Gulf of Finland,” *Remote Sensing of Environment*, 113, 2574-2591, 2009.

G. Zibordi, F. Mélin, J.-F. Berthon, and E. Canuti, “Assessment of MERIS ocean colour data products for European seas,” *Ocean Sciences*, 9, 521–533, 2013.

G. Zibordi, C. J. Donlon, and A. C. Parr, “*Optical radiometry for ocean climate measurements in Experimental Methods in the Physical Sciences,”* Vol. 47. Academic Press, 2014.

G. Zibordi and K. J. Voss, “*In situ* optical radiometry in the visible and near infrared. In *Optical Radiometry for Oceans Climate Measurements, Experimental Methods in the Physical Sciences volume 47,”* G. Zibordi, C. Donlon and A. Parr Ed.s, Elsevier - Academic Press, Amsterdam, 2014.

List of acronyms

AAOT	Acqua Alta Oceanographic Tower
AE	Adjacency Effects
AERONET-OC	Ocean Colour component of the Aerosol Robotic Network
ARTEMIS-OC	Advanced Radiative Transfer Models for In-situ & Satellite Ocean Colour data
BioMaP	Bio-optical mapping of Marine optical Properties
BLKS	Black Sea
CDR	Climate Data Record
DDS	Diagnostic Data Sets
EMED	Eastern Mediterranean Sea
EUMETSAT	European Organization for the Exploitation of Meteorological Satellites
FEMRAD-OC	Finite Element method for the simulation of Ocean Colour satellite data
FR	Full Resolution
HLT	Helsinki Lighthouse Tower
GAC	Global Acquisition Area
GDLT	Gustaf Dalen Lighthouse Tower
GLR	Gloria platform
GLT	Galata platform
HIP	HPLC Inter-comparison of Pigments
HPLC	High Pressure Liquid Chromatography
ISHL	Iberian Shelf Sea
LAC	Local Acquisition Area
MERIS	MEdium Resolution Imaging Spectrometer
MODIS-A	Medium Resolution Imaging Spectrometer on-board the Aqua platform
MODIS-T	Medium Resolution Imaging Spectrometer on-board the Terra platform
MSI	MultiSpectral Instrument
NAUSICAA	Novel Adjacency Perturbation Simulator for Coastal Areas
NL	Noise Level
NPP	National Polar-Orbiting Partnership
OLCI	Ocean and Land Colour Instrument
RR	Reduced Resolution
RTM	Radiative Transfer Model
SCOR	Scientific Committee on Oceanographic Research
SeaDAS	SeaWiFS Data Analysis System
SeaHARRE	SeaWiFS HPLC Analysis Round-Robin Experiment
SeaWiFS	Sea-viewing Wide Field-of-View Sensor
SVC	System Vicarious Calibration
SWIR	Short Wavelength Infrared
VIIRS	Visible Infrared Imaging Radiometer Suite

GETTING IN TOUCH WITH THE EU

In person

All over the European Union there are hundreds of Europe Direct information centres. You can find the address of the centre nearest you at: https://europa.eu/european-union/contact_en

On the phone or by email

Europe Direct is a service that answers your questions about the European Union. You can contact this service:

- by freephone: 00 800 6 7 8 9 10 11 (certain operators may charge for these calls),

- at the following standard number: +32 22999696, or

- by electronic mail via: https://europa.eu/european-union/contact_en

FINDING INFORMATION ABOUT THE EU

Online

Information about the European Union in all the official languages of the EU is available on the Europa website at: https://europa.eu/european-union/index_en

EU publications
You can download or order free and priced EU publications from EU Bookshop at: https://publications.europa.eu/en/publications. Multiple copies of free publications may be obtained by contacting Europe Direct or your local information centre (see https://europa.eu/european-union/contact_en).

KJ-NA-29476-EN-N

The European Commission's science and knowledge service

Joint Research Centre

JRC Mission

As the science and knowledge service of the European Commission, the Joint Research Centre's mission is to support EU policies with independent evidence throughout the whole policy cycle.

EU Science Hub

ec.europa.eu/jrc

@EU_ScienceHub

EU Science Hub - Joint Research Centre

Joint Research Centre

EU Science Hub

Publications Office

doi:10.2760/203446

ISBN 978-92-79-98109-8